Beyond Hodgkin–Huxley: The Ionic-Mechano-Hydraulic (IMH) Model of Nerve Conduction

Bernard Delalande [*,†], Hirohisa Tamagawa [†], Vladimir Matveev [†]

Posted Date: 27 April 2026

doi: 10.20944/preprints202603.0725.v6

Keywords: action potential; hydraulic wave; polyelectrolyte gel; Donnan equilibrium; myelin; mechanoreceptor

 doi:10.20944/preprints202603.0725.v6

Article

Beyond Hodgkin–Huxley: The Ionic-Mechano-Hydraulic (IMH) Model of Nerve Conduction

Bernard Delalande [1,2,*,†], Hirohisa Tamagawa [2,†] and Vladimir Matveev [3,†]

[1] 280, avenue de la Pierre Dourdant, 38290 La Verpilliere, France
[2] Department of Mechanical Engineering, Faculty of Engineering, Gifu University, 1-1 Yanagido, Gifu, Gifu, 501-1193 Japan
[3] Laboratory of Cell Physiology, Institute of Cytology, Russian Academy of Sciences, Tikhoretsky Ave 4, St. Petersburg 194064, Russia
* Correspondence: bernard@somasimple.com
† These authors contributed equally to this work.

Abstract

The axonal membrane is not the seat of nerve conduction: it is the boundary between two osmotic reservoirs whose asymmetry is the thermodynamic engine of the action potential. Voltage-gated ion channels are not the generators of the nerve signal: they are its osmotic amplifiers, and their spatial distribution along the axon is a geometric necessity, not an arbitrary anatomical feature. The Ionic-Mechano-Hydraulic (IMH) model formalises this principle: intracellular K^+ adsorbed on the cytoplasmic polyelectrolyte gel triggers an ionic phase transition; extracellular Na^+ amplifies the resulting hydraulic wave through Nav channels; Kv channels close the osmotic cycle and enforce the refractory period. The conduction velocity is predicted from the elastic modulus of myelin, not from the density of the sodium channel. The model resolves a 75-year-old anomaly that Huxley and Stämpfli themselves described as impossible in a purely electrical system: a positive current enters a node before the membrane potential at the preceding node has reached its maximum. Ten falsifiable predictions are presented that cover myelin mechanics, mechanoreceptor adaptation, terminal arborisation geometry, velocity-diameter scaling, and axon diameter limits derived from first physical principles. The Hodgkin-Huxley model is not discarded: it is explained.

Keywords: action potential; hydraulic wave; polyelectrolyte gel; Donnan equilibrium; myelin; mechanoreceptor

---

"Simplicity is the ultimate sophistication." —Leonardo da Vinci

"Everything should be made as simple as possible, but not simpler." —Albert Einstein

1. Introduction

The Hodgkin-Huxley (HH) equations, published in 1952, provide a quantitative description of the action potential that remains the foundation of computational neuroscience [3]. Their predictive power is not in question. What is in question is their physical interpretation.

Hodgkin and Huxley were explicit on this point:

"**We do not wish to suggest that the equations we have used [...] necessarily bear any close relationship to the actual physical process involved.**"

The equations are a phenomenological fit to the data obtained from a specific preparation: the denudated giant squid axon with a replaced axoplasm [4]. Baker, Hodgkin, and Shaw demonstrated that action potentials persist after axoplasm replacement with saline, and concluded, without further experimental tests, that the eliminated components were functionally neutral. The IMH model (Ionic-Mechano-Hydraulic: ionic gel phase transition as the primary event, mechanical compression as the trigger, and hydraulic wave propagation as the conduction mechanism) proposes that this conclusion

 doi:10.20944/preprints202603.0725.v6

was incorrect and that the cytoplasmic gel, structured water, adsorbed ions, and phase transitions eliminated by the preparation are the primary mechanism of conduction. We hereafter use the acronym IMH to emphasise the causal hierarchy: ionic desorption precedes and causes the mechanical and hydraulic events that follow.

The genealogy of the dominant model contains two earlier assumptions that deserve scrutiny. In 1902, Julius Bernstein applied the Nernst equation to quantify the resting membrane potential [2], on the advice of Wilhelm Ostwald. The Nernst equation is rigorously valid only for a single ion species across an ideal semipermeable membrane under thermodynamic equilibrium [1] – conditions that the axonal cytoplasm does not satisfy. This application was a convenient approximation that was never validated in the biological context; it was adopted and transmitted. The HH model inherits this unverified foundation.

A further structural issue concerns the preparation itself. Young (1936) established that the giant squid axon is not a single axon but a developmental fusion of hundreds of smaller axons [5], with an uncharacterised internal hydraulic architecture. The canonical preparation of twentieth-century electrophysiology was therefore neither structurally representative nor simple.

The need to move beyond HH is now recognised within mainstream modelling.

Peets, Tamm, and Engelbrecht (2023), reviewing the state of mathematical models of nerve signal propagation, explicitly call for the incorporation of the cytoskeleton as a potentially primary actor, citing evidence that its removal alters the response to axoplasmic pressure by an order of magnitude [21]; they conclude that the cytoskeleton could prove "**as important for signal propagation in nerves as the cell membrane.**" Most recently, Tamm, Peets, and Engelbrecht (2026) introduced a phenomenological inductance term to render the HH equation hyperbolic, acknowledging that the parabolic formulation is physically inadequate for wave propagation [42]. The IMH model is hyperbolic by construction, through the Moens-Korteweg equation for a fluid-filled elastic tube, without requiring additional parameters.

Drukarch and Wilhelmus (2023) identify the top-down thermodynamic approach, treating the nerve signal as emerging from the collective physico-chemical properties of the axolemma-ectoplasm complex, as the necessary direction for a mechanistically complete account [23].

The IMH model answers both calls by providing the physical account of the medium in which the nerve signal propagates: the axonal membrane is not the seat of conduction but the boundary between two osmotic reservoirs, and voltage-gated channels are not the generators of the action potential but its osmotic amplifiers. The biophysical foundations of this model are developed in Section 2.

The present work does not propose to discard the HH model. It proposes to explain it: to identify the physical substrate from which its equations emerge as a first-order projection, and to provide the mechanistic account its authors called for.

Section 3 presents convergent evidence from independent experimental observations.

Section 4 states falsifiable predictions.

The evolutionary context and the relationship with alternative non-HH frameworks are developed in Section 5.

The Discussion and Conclusions assess the relationship between the two frameworks.

2. The IMH Model

2.1. The Cytoplasmic Gel: Ling's Foundation

Gilbert Ling demonstrated that the cytoplasm is a structured polyelectrolyte gel in which the majority of the intracellular K^+ is adsorbed at the protein sites rather than dissolved in a free solution [6]. The resting ionic distribution is a thermodynamically stable Donnan equilibrium, expressed in equation (1), where R is the gas constant, T the absolute temperature, F the Faraday constant, and the ratio in brackets is the K^+ concentration gradient across the gel boundary:

$$E_{\text{Donnan}} = -\frac{RT}{F} \ln\left(\frac{[K^+]_{\text{in}}}{[K^+]_{\text{out}}}\right) \tag{1}$$

 doi:10.20944/preprints202603.0725.v6

Equation (1) differs from the Nernst equation in a critical respect: it describes a true thermodynamic equilibrium of the gel system as a whole, not a single-ion diffusion potential across an ideal membrane. This equilibrium is the energetically favourable state of the charged gel; it requires no metabolic pump to be maintained. Tamagawa formalised this framework in rigorous thermodynamic terms and quantitatively demonstrated that observed membrane potentials are consistent with Donnan equilibrium without pump-dependent gradient maintenance [7]. In this sense, the Na^+ / K^+-ATPase pump performs a regulatory and not a primary electrogenic function.

The Ling polyelectrolyte gel framework is based on colloid science and the thermodynamics of charged polymer networks – a field with rigorous theoretical foundations, a well-established mathematical formalism, and extensive industrial validation in materials science, food science, and polymer physics. Flory-Huggins theory, Donnan equilibrium, and Langmuir adsorption isotherms are not biological hypotheses: they are physical laws whose validity in non-biological systems is uncontested. Ling's contribution was to recognise that the living cytoplasm satisfies the conditions for these laws to apply, a recognition that has been marginalised within electrophysiology for reasons of disciplinary sociology rather than physical evidence.

The adsorption of K^+ at gel sites follows a Langmuir isotherm, with affinity constants ordered by the Hofmeister ion series [8]. In equation (2), N is the total density of the adsorption sites, K_a is the adsorption affinity constant for K^+ and $[K^+]_{\text{free}}$ is the concentration of unbound K^+ in the gel interstitium:

$$[K^+]_{\text{ads}} = \frac{N \cdot K_a \cdot [K^+]_{\text{free}}}{1 + K_a \cdot [K^+]_{\text{free}}} \tag{2}$$

Equation (2) has a direct physical consequence: when mechanical compression increases $[K^+]_{\text{free}}$ locally, the isotherm shifts and the adsorption sites become transiently saturated, releasing a pulse of free K^+ into the periaxonal space. This pulse is the ionic trigger of the hydraulic wave.

2.2. The Hydraulic Wave

Mechanical compression of the axon triggers the desorption of K^+ from the gel sites. Desorbed ions reconstruct their hydration shells, generating a local osmotic pressure gradient and hydraulic flux. A pressure wave propagates in the periaxonal space (12–15 nm width) at a velocity governed by the Moens-Korteweg equation adapted for a fluid-filled elastic tube of small radius:

$$v = \sqrt{\frac{K_{\text{eff}}}{\rho}} \tag{3}$$

$$K_{\text{eff}} = \left(\frac{1}{K_{\text{fluid}}} + \frac{2r}{E_{\text{myelin}} \cdot h} \right)^{-1} \tag{4}$$

where E_{myelin} is the elastic modulus of the myelin sheath, r is the radius of the periaxonal canal, h is the thickness of the sheath, K_{fluid} is the bulk modulus of the periaxonal fluid and ρ is its density. Equation (4) contains the central experimental prediction of the model: *the conduction velocity is determined by the elastic modulus of myelin, not by the density of the sodium channel.*

The Heimburg-Jackson thermodynamic soliton model established that the lipid membrane near a phase transition supports mechanically reversible wave propagation [9]. The IMH model integrates this as a component of a three-way thermal balance, expressed in equation (5), where the three terms represent, respectively, the heat absorbed by the membrane lipid phase transition, the heat released by K^+ adsorption onto gel sites during recovery, and the heat exchanged with the structured water shell surrounding the desorbed ions.

$$\Delta Q_{\text{total}} = \Delta Q_{\text{lipid}} + \Delta Q_{\text{gel}} + \Delta Q_{\text{water}} \approx 0 \tag{5}$$

 doi:10.20944/preprints202603.0725.v6

The near-zero net heat exchange measured during the action potential [12] is a thermodynamic constraint. Equation (5) satisfies it by construction because the three contributions are thermodynamically coupled and partially cancel: what the membrane lipid phase transition absorbs, the gel recovery releases. The HH model, which is irreversible by design, does not account for this constraint.

2.3. The Role of Voltage-Gated Channels: Osmotic Amplifiers of the Hydraulic Wave

The IMH model does not remove voltage-gated ion channels from the description of nerve conduction. It redefines their functional role: the Nav and Kv channels are osmotic amplifiers of the hydraulic wave, not its primary generators.

The distinction between K^+ and Na^+ as actors in this amplification follows directly from the Hofmeister series and the gel framework of Ling. K^+ has a higher adsorption affinity for intracellular protein sites than Na^+; Na^+ therefore remains predominantly free in the extracellular periaxonal space, where it is present at 145 mM – approximately 29 times the extracellular K^+ concentration. This large extracellular Na^+ reservoir constitutes an immediately available osmotic energy source that requires no metabolic expenditure to maintain.

The functional role of these channels is most clearly seen in the ancestral case: the unmyelinated fibre, which predates myelination by more than 500 million years and remains the sole axonal architecture in invertebrates, in the entire pre-vertebrate lineage, and in a substantial fraction of the vertebrate peripheral and central nervous systems. In an unmyelinated axon, Nav and Kv channels are continuously distributed along the axonal membrane. As the hydraulic wavefront propagates, local mechanical deformation of the membrane opens the Nav channels along its path; the resulting Na^+ influx amplifies the local osmotic pressure in the periaxonal space and sustains the amplitude of the wave against viscous dissipation. Nav channels thus serve the same amplification function as Ca^{2+} desorption in the cnidarian nematocyst [14]: an extracellular ion reservoir is mobilised to support the propagating hydraulic event, in a geometry that is spatially distributed and continuous. The Kv channels open in temporal opposition to the Nav channels, producing an efflux of K^+ that reverses the local increase in osmotic pressure and restores the segment of periaxonal space immediately behind the wavefront to its resting state. The Nav/Kv opposition is therefore not a competition for membrane potential control but a *compression–decompression cycle* that maintains the waveform and enforces the refractory period: while Kv remains open and the local periaxonal pressure is dissipating, Nav cannot reopen – the osmotic geometry of the canal prevents it. The absolute refractory period corresponds to the Kv-open phase; the relative refractory period corresponds to the partial recovery phase during which a stronger-than-normal hydraulic stimulus can still initiate a wave of reduced amplitude.

Myelination, which appears in the gnathostome lineage, is a later and concurrent engineering solution superimposed on this ancestral architecture. The amplification principle is conserved; the geometry of its deployment is transformed. In the myelinated fibre, the insulating sheath suppresses transmembrane ionic exchange along the internode and confines the opportunity for amplification to the Ranvier nodes. When the hydraulic wavefront reaches a node, the mechanical deformation of the nodal membrane opens the high-density Nav channels clustered there; the resulting Na^+ influx delivers a discrete osmotic amplification pulse that recharges the amplitude of the hydraulic wave before it traverses the next internode. The Kv channels, concentrated at the juxtaparanodal regions immediately downstream of each node, close the osmotic cycle at the corresponding location and ensure that recovery is completed before the wave reaches the next node. The spatial segregation of Nav and Kv in myelinated fibres is therefore not an arbitrary anatomical feature, and it is not a design principle newly introduced by myelination: it is the geometric relocation of the same distributed compression–decompression cycle already operating in the ancestral unmyelinated fibre, reorganised in space to match the discrete topology imposed by the insulating sheath.

The pharmacological evidence is consistent with this reinterpretation in both architectures. Tetrodotoxin (TTX), which blocks Nav channels, abolishes the electrically recorded action potential and eventually blocks conduction because, without Nav-mediated osmotic amplification, the hydraulic wave attenuates progressively along the axon and fails to reach threshold – distributed

 doi:10.20944/preprints202603.0725.v6

along the membrane in unmyelinated fibres, at successive nodes in myelinated fibres. Under partial TTX block, the IMH model predicts a graded reduction in conduction distance before complete block, rather than an all-or-nothing threshold effect, a prediction distinguishable from the HH expectation that conduction either succeeds or fails at each point (unmyelinated) or at each node (myelinated) independently.

2.4. The Universal Sigmoid as Gel Thermodynamics

Every known biological sensory receptor—mechanoreceptor, photoreceptor, nociceptor, thermoreceptor, and chemoreceptor—exhibits a sigmoidal stimulus-response curve. In the HH framework, this universality requires a separate molecular justification for each receptor class. In the IMH model, it is a necessary consequence of polyelectrolyte gel thermodynamics, expressed in equation (6), where $R(S)$ is the receptor response as a function of stimulus intensity S, $R_{\max}$ is the maximum response, $S_{\text{threshold}}$ is the activation threshold, and k is the slope parameter governing transition sharpness:

$$R(S) = \frac{R_{\max}}{1 + e^{-k(S - S_{\text{threshold}})}} \tag{6}$$

Equation (6) is not fitted to receptor data post-hoc: its three parameters are determined independently by the physical properties of the gel. $S_{\text{threshold}}$ is the minimum compression for a self-sustaining hydraulic wave (a geometric condition of the periaxonal canal); k is the gel surface-to-volume ratio; and $R_{\max}$ is determined by the total density of the adsorption sites. The sigmoid emerges from gel thermodynamics, not from curve fitting. The diversity of receptors between species reflects the diversity of hydraulic architectures, not the diversity of molecular transduction mechanisms. This reformulates von Uexküll's Umwelt principle [15] in biophysical terms: the perceptual world of each species is the hydraulic geometry of its peripheral nervous system made accessible to it.

2.5. The Axon-Schwann Cell Couple as Hydraulic Waveguide

The key architectural unit of the IMH model is not the axon in isolation but the axon-Schwann cell couple. Santiago Ramón y Cajal's neuron doctrine (1906), while correct regarding synaptic connectivity, imposed an analytical separation of the axon from its Schwann cell that made the periaxonal space conceptually invisible. The Schwann cell is not passive support: it provides the elastic wall of the hydraulic tube and contributes to the regulation of periaxonal ionic composition. Pannese documented the structural continuity of this couple in detail [16] and established a point of anatomical fact that is central to the IMH framework: *every* axon of the vertebrate peripheral nervous system is ensheathed by Schwann cells, and every axon of the central nervous system is ensheathed by oligodendrocyte processes or astrocytic contacts. The naked axon does not exist in situ. In myelinated fibres, a single Schwann cell (PNS) or oligodendrocyte process (CNS) wraps the axon in a multi-lamellar spiral of compacted membrane, producing the thick dielectric sheath classically associated with saltatory conduction. In unmyelinated fibres, multiple axons are embedded together in the cytoplasm of a single Schwann cell that forms a non-compacted envelope around each one – the Remak bundle [16]. In both cases, a periaxonal space of controlled geometry is defined between the axolemma and the glial envelope, and in both cases this space is bounded by an elastic cellular wall. Figure 1 illustrates this shared architecture: both the Remak bundle (panel a) and the myelinated fibre (panel b) are enclosed by a continuous basal lamina, and in both cases a periaxonal space is defined between the axolemma and the surrounding glial envelope. The basal lamina is a constant external boundary of the axon-glia couple; the myelin sheath, when present, is an internal mechanical optimisation of a pre-existing hydraulic architecture, not the defining element of it.

 doi:10.20944/preprints202603.0725.v6

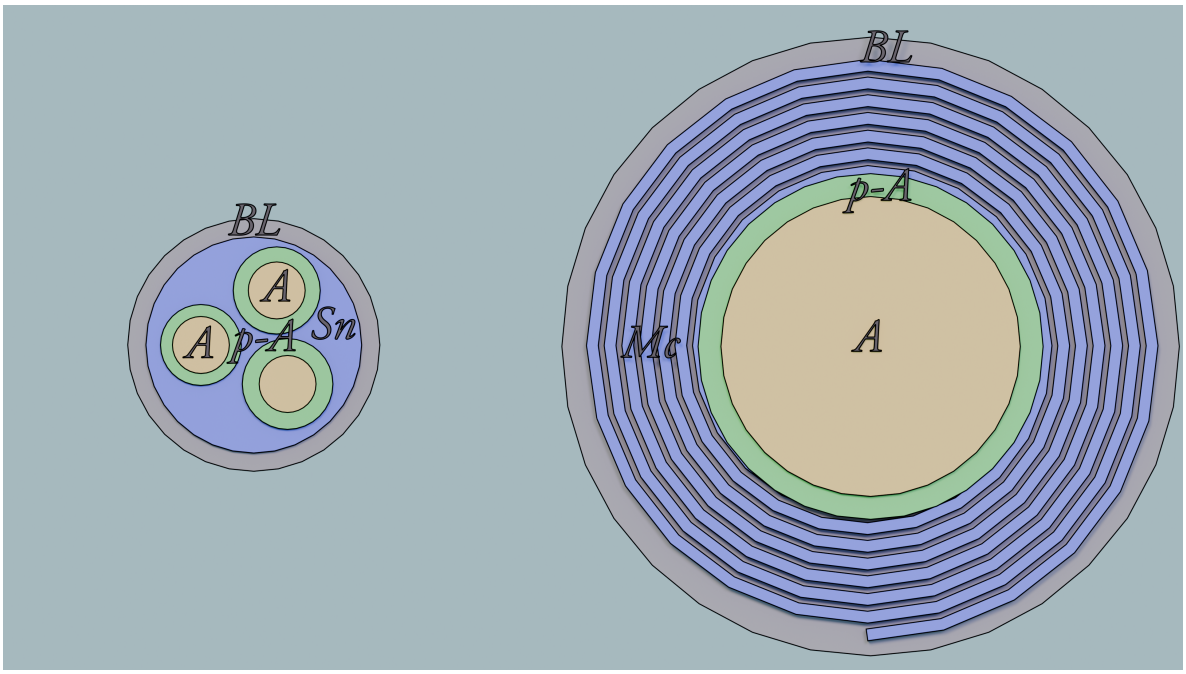

Figure 1. Comparative anatomy of the axon-glia couple in unmyelinated (a, left) and myelinated (b, right) fibres. **(a) Remak bundle.** Several small-calibre axons (A) are embedded in the cytoplasm of a single Schwann cell (Sn, non-compacted), each in its own periaxonal channel (p-A); the whole assembly is enclosed by a continuous basal lamina (BL). **(b) Myelinated fibre.** A single axon (A) is wrapped by the compacted plasma membrane of one Schwann cell (in the peripheral nervous system) or one oligodendrocyte process (in the central nervous system), forming compact myelin (Mc) with a periaxonal space (p-A) of controlled width (approximately 12 nm internodally) maintained between the axolemma and the innermost glial lamella; the whole is enclosed by a basal lamina (BL). In both architectures the axon is bounded by (i) its own axolemma, (ii) a periaxonal space (p-A), (iii) a glial envelope (Sn, non-compacted, in (a); Mc, compacted, in (b)), (iv) a continuous basal lamina (BL). The IMH hydraulic waveguide is a property of this shared architecture, not of myelination specifically. Myelination stiffens the elastic wall and accelerates the Moens–Korteweg wave; it does not create the waveguide. Schematic representation; relative scales between the two panels are illustrative.

The IMH hydraulic waveguide is therefore not a property specific to myelination: it is a property of the axon-glia couple as such. What differs between architectures is the mechanical specification of the wall, the effective elastic modulus of the wall, which we continue to denote E_{myelin} in equation (4) for continuity with the classical literature, although in unmyelinated fibres it refers to the combined modulus of the axolemma and the non-compacted Schwann envelope, not the existence of the waveguide. The thin, non-compacted Schwann envelope of a Remak bundle has a lower effective modulus than the thick, compacted myelin sheath of a large peripheral fibre; the Moens–Korteweg velocity is correspondingly lower in unmyelinated fibres, as observed.

The elastic wall of the hydraulic waveguide is in fact a composite structure in both architectures. In the Remak bundle and in the myelinated fibre alike, the wall consists of the glial envelope (non-compacted Schwann cytoplasm in the unmyelinated case, compacted myelin in the myelinated case) and the continuous basal lamina that encloses the axon–glia couple externally. The effective wall stiffness that enters the Moens–Korteweg relation is therefore a sum of contributions, not a single-layer modulus:

$$E_{\text{eff}} \cdot h_{\text{eff}} = E_{\text{glial}} \cdot h_{\text{glial}} + E_{\text{lamina}} \cdot h_{\text{lamina}} \tag{7}$$

in which the contribution of the basal lamina is minor in absolute terms but not negligible, and becomes proportionally more important in small-calibre fibres where h_{glial} is itself small. Rosso et al. [55] provided a direct demonstration of this composite structure in the peripheral nervous system: the mechanical resilience of the myelinated fibre is not governed by the myelin sheath alone, but by the base lamina of the Schwann cell together with PMP22, whose removal severely compromises the

 doi:10.20944/preprints202603.0725.v6

mechanics of the fibre despite the myelin remaining intact. This finding is orphan in the HH framework – the basal lamina has no role in a purely electrical account of conduction – but it is a direct prediction of the IMH framework, in which the basal lamina is the external structural element of the hydraulic waveguide. A corollary follows for pathology: partial demyelination reduces E_{myelin} but leaves E_{lamina} intact, so the stiffness of the composite wall is reduced but not destroyed. The IMH model therefore predicts that demyelination should produce graded conduction slowing, not binary conduction failure – consistent with what is clinically observed in multiple sclerosis and other demyelinating diseases, and in agreement with the in vitro quantification of axonal viscoelasticity in demyelinated tissue [56].

Myelination is, in this reading, a mechanical optimisation of a pre-existing hydraulic architecture: it stiffens the elastic wall to accelerate the wave, it does not create the wall. A century of electrophysiology conducted on the isolated axon –with the elastic wall removed, the periaxonal space disrupted, and the gel replaced – was conducted on half of the functional unit, without ever testing whether the other half was neutral. Beaudoin et al. [44] have recently synthesised the structural biology of this couple under the heading of *structural electrobiology*, emphasising, in the myelinated case, that the periaxonal space is maintained at a precisely controlled width by a dedicated molecular architecture: Caspr1–contactin–neurofascin-155 septate-like junctions at the paranodes, Caspr2–TAG-1 complexes at the juxtaparanodes, and MAG–ganglioside and nectin-like interactions stabilising the internodal width. This architecture is geometrically incompatible with the notion of a passive extracellular gap. In the HH framework, the functional role of this precision remains unexplained; in the IMH model, it is a direct structural requirement: a hydraulic waveguide must have a controlled lumen and the periaxonal width is that lumen. Cohen et al. [43] provided the corresponding functional measurement, combining voltage-calibrated optical recording at high temporal resolution, electron microscopy, and constrained cable modelling in neocortical pyramidal axons to demonstrate that the periaxonal space is a continuous longitudinal pathway, incompletely sealed at the paranodes, participating directly in the spatial and temporal profile of the action potential. Their identification of a "double-cable" internodal geometry, with the axolemma and myelin sheath separated by a submyelin conductor, experimentally establishes the periaxonal space as a physically distinct compartment along the axon, the same compartment that the IMH model identifies as the hydraulic waveguide. The convergence is structural and geometric, and is independent of the interpretive framework applied to it: the existence of a narrow, longitudinally continuous, electrically, and chemically distinct periaxonal channel is now experimentally established at the single-axon level.

The biophysical nature of the glial envelope itself has been independently elucidated by three converging lines of experimental work that together place myelin in a specific class of materials: a polyelectrolyte hydrogel assembled by an electrostatically-triggered phase transition, mechanically coupled to a dynamically regulated cortical actin network, and spatially organised by a polarised trafficking architecture. At the molecular level, Aggarwal et al. [45] demonstrated that the myelin basic protein (MBP), an intrinsically disordered protein with a net charge of $+20$ at physiological pH, undergoes a reversible phase transition into a functional amyloid-like meshwork upon binding to the inner leaflet of the myelin membrane. The transition is triggered by charge neutralisation by anionic lipids, proceeds through phenylalanine-mediated hydrophobic interactions, and produces a size-selective semipermeable network biophysically comparable to the FG-repeat hydrogel of the nuclear pore [50]. At the cytoskeletal level, Zuchero et al. [46] and Nawaz et al. [47] showed that MBP, by binding the same membrane PI(4,5)P_2 with very high affinity, competes the actin-disassembly factors cofilin and gelsolin off the lipid, releasing them to depolymerise F-actin at the inner tongue; active myelin wrapping is therefore driven by regulated actin disassembly, not polymerisation. At the architectural level, Snaidero et al. [48] reconstructed the three-dimensional organisation of the growing sheath by high-pressure freezing electron microscopy and serial block-face imaging, revealing a system of cytoplasmic channels that traverse the compact layers and connect the outer tongue to the inner tongue at the axolemmal interface; these channels close with maturation but can be reopened in adulthood by elevation of PI(3,4,5)P_3, reinitiating myelin growth. These results place

 doi:10.20944/preprints202603.0725.v6

the myelin sheath in the same biophysical class as the nuclear pore hydrogel and other intrinsically-disordered-protein phase separations, and they establish that the periaxonal compartment is flanked by a structured polyelectrolyte phase whose state is electrostatically regulated on physiological timescales. The IMH polyelectrolyte gel at the axolemmal interface is therefore not an exotic postulate but a documented class of biophysical object, at work in the immediately adjacent compartment, through well-characterised molecular machinery.

Four further features of this architecture, established by the same body of work, sharpen its incompatibility with the textbook image of myelin as a passive dielectric insulator and bring it into direct correspondence with the IMH framework. First, the inner tongue is not a static apposition to the axolemma, but an actively trafficked membrane domain: Snaidero et al. [48] demonstrated by VSV-G pulse-chase that newly synthesised membrane proteins are delivered to the inner tongue via the polarised biosynthetic pathway, establishing the periaxonal interface as a continuously supplied compartment rather than a sealed gap. Second, the inner tongue is enriched in F-actin during active myelination (P4) and progressively depleted of it at maturity (P60) [46,48], identifying a developmental mechanical signature of the wrapping process at the same interface where the IMH framework locates the hydraulic periaxonal event; in a purely dielectric reading of the sheath, no specific cytoskeletal signature for the inner tongue should exist or vary with developmental stage. Third, Snaidero et al. [48] reinterpreted myelin outfolds, long classified as pathological, as transient physiological membrane reservoirs during active wrapping, demonstrating that the sheath accommodates volume and surface fluctuations on physiological timescales, a property compatible with a hydraulically loaded compartment but not motivated by the static-insulator picture. Fourth, Velumian, Samoilova, and Fehlings [49] provided the direct fluid-dynamic confirmation of the cytoplasmic continuum implied by the Snaidero channels: microinjection of the small fluorescent tracer Lucifer Yellow into a single point of a living myelin sheath demonstrated rapid diffusion through the entire cytoplasmic network, from the outer to the inner tongue, across the compact layers, in white matter axons of mature CNS tissue. The myelin sheath surrounding the axon is therefore a continuously connected cytoplasmic compartment, mechanically loaded, actively supplied, and remodelable on physiological timescales, precisely the structural specification required by the IMH model for the elastic wall of the hydraulic waveguide and incompatible with the cable-theory specification of myelin as a passive dielectric layer.

A fourth quantitative line of evidence completes this picture. Chuang et al. [54] used atomic force microscopy (AFM, PeakForce QNM mode) with in situ fluorescent immunocytochemistry on primary dorsal root ganglion / oligodendrocyte co-cultures to measure, on the same axon, the viscoelastic response of myelinated and adjacent unmyelinated segments. The design separates the contribution of myelination from every confounding variable that tissue-level work cannot disentangle. Two results are directly relevant to the IMH framework. First, the Young's modulus of the myelinated segment is significantly greater than that of the adjacent unmyelinated segment on the same axon, rising from approximately 3.4 kPa to approximately 3.8 kPa, with $p < 0.0001$ at all developmental time points; the correlation between the local myelin ratio and the local modulus is significant ($p = 0.001$). Second, and more consequentially for the IMH reading, the rheological response is governed by a two-element Maxwell model with two characteristic relaxation times: a long relaxation time $\tau_1 \approx 2.5$ s that is invariant with myelination ($p = 0.132$ between slopes), and a short relaxation time $\tau_2 \approx 0.5$ s that decreases significantly with myelination ($p < 0.0001$ between slopes). The authors assign τ_1 to the cytoskeletal compartment (comparable in magnitude to cytoskeletal relaxation reported in previous work) and τ_2 to the membrane compartment (comparable to the ~ 0.3 s relaxation of red blood cell membranes without cytoskeleton reported by Evans and Hochmuth 1976). This experimental dissociation is central. The IMH framework distinguishes, on physical grounds, two compartments with different mechanical identities: the cytoplasmic polyelectrolyte gel, whose long-time behaviour is dominated by the actin-spectrin cortex (and is therefore expected to be invariant under changes that do not affect the cytoskeleton), and the glial envelope functioning as the elastic wall of the hydraulic waveguide (whose stiffness is specifically modified by myelination). The Chuang 2023 dissociation – τ_1

 doi:10.20944/preprints202603.0725.v6

invariant, τ_2 myelination-dependent – is the direct rheological signature of this distinction. In the HH framework, no such dissociation is expected or explained: the myelin sheath is purely dielectric, and no rheological signature specific to myelination should emerge. The measurement therefore supplies both a quantitative anchor in the kPa / hundreds-of-milliseconds range for the IMH hydraulic framework and an experimental signature that discriminates between the two models on terms specifiable in advance.

2.6. The Saline Resistivity Argument

The "double-cable" framework inherited from classical cable theory treats the periaxonal space as a thin longitudinal saline conductor between the axolemma and the myelin sheath [43]. In that reading, the space functions as a passive return path for transmembrane currents during the action potential. A quantitative examination of this assumption, using the dimensions established by electron microscopy and the known resistivity of extracellular saline, shows that it is physically incompatible with the geometry itself. The internodal periaxonal width has been measured at approximately 12 nm [44]; a representative internodal length is of the order of 100 μm; a typical axon calibre is of the order of 1 μm. The periaxonal compartment therefore forms an annular cylinder of inner radius $r \approx 500$ nm, thickness $h \approx 12$ nm, and length $L \approx 100$ μm, enclosing a total conducting cross-section of $A = 2\pi rh \approx 3.8 \times 10^{-14}$ m^2. With physiological extracellular resistivity $\rho \approx 0.7$ Ω·m and length $L = 10^{-4}$ m, the longitudinal resistance of this putative saline pathway is

$$R_{\text{periaxonal}} = \rho\, L / A \approx 1.8 \times 10^{9}\ \Omega \tag{8}$$

per internode, that is, approximately two gigaohms. For comparison, the axoplasmic core of the same internode, with resistivity $\rho_{\text{axon}} \approx 0.7$ Ω·m and cross-section $\pi r^2 \approx 8 \times 10^{-13}$ m^2, has a longitudinal resistance of approximately 90 MΩ, a factor of twenty lower. A current required to flow through the periaxonal pathway in order to close a passive return circuit would encounter, per internode, an impedance comparable to the membrane resistance itself. A cable model that treats this pathway as a low-impedance saline conductor is, at these dimensions, not quantitatively viable. The difficulty is compounded by the behaviour of aqueous electrolytes under nanometric confinement: at channel widths below approximately 10 nm, the effective conductivity of saline decreases by roughly an order of magnitude relative to the bulk, as surface conduction, counterion condensation, and confined-water effects become dominant and bulk electroneutrality is violated. In this regime a 12 nm periaxonal gap is present; equation (8) is, if anything, optimistic.

Two alternative interpretations of the space are consistent with its measured dimensions. The first is that the compartment is not a conductor but a structured hydrogel, whose fixed charges and bound water dominate ionic transport (the IMH reading, consistent with the polyelectrolyte phase documented in the adjacent cytoplasmic leaflet by Aggarwal et al. [45]). The second is that the compartment serves a non-electrical function, mechanical, chemical, or osmotic, in which case its role in the saltatory mechanism must be reformulated from first principles. In either case, the assumption that a 12 nm saline gap carries the axial return current of a classical cable model is inconsistent with the measured geometry and with the nanofluidic behaviour of electrolytes at that scale. The IMH framework does not reject the geometry; it reinterprets it as the lumen of a hydraulic waveguide, in which force is carried by pressure rather than by net charge transfer, a role for which the measured dimensions are entirely adequate.

3. Convergent Evidence

3.1. Huxley and Stämpfli 1949: The Anomaly That Was Named and Left Unexplained

In their study of saltatory conduction in the sciatic nerve of frogs, Huxley and Stämpfli recorded a result they described in their own words as "**impossible in a resistance and capacity system**" [10]: a positive current entered the axis cylinder at node $N{+}1$ *before* the membrane potential at node N had reached its maximum. This directly contradicts the temporal logic of any RC-based propagation

 doi:10.20944/preprints202603.0725.v6

model, in which the downstream node can only be activated after the upstream node has completed depolarisation.

The arithmetic clarifies the constraint. For a frog sciatic nerve with conduction velocity $v = 60\,\mathrm{m/s}$ and internodal length $L = 1\,\mathrm{mm}$:

$$\Delta t_{N\to N+1} = \frac{L}{v} = \frac{1\times10^{-3}}{60} \approx 17\,\mu\mathrm{s} \tag{9}$$

The duration of the action potential at a single node is approximately 1 ms. Node $N{+}1$ therefore activates when node N has consumed only:

$$\frac{\Delta t}{\tau_{\mathrm{AP}}} = \frac{17\,\mu\mathrm{s}}{1000\,\mu\mathrm{s}} = 0.017 \tag{10}$$

That is, 1.7% of its duration of action potential. In the electrical model, this requires that node N generates sufficient axial current within 17 μs to depolarise node $N{+}1$ past the threshold, a demand inconsistent with the measured RC time constants of the nodal membrane. In the IMH model, the periaxonal pressure wave arrives at node $N{+}1$ in 17 μs independently of the electrical state of node N, because the wave is the primary event and the electrical response is its consequence. This result is not specific to the sciatic nerve of the frog. For any myelinated fibre, the inter-nodal transit time $\Delta t_{N\to N+1} = L/v$ must be compared with the duration of the action potential τ_{AP} at a single node.

$$\frac{L}{v} < \tau_{AP} \tag{11}$$

Whenever node $N+1$ is activated before the action potential at node N is completed. This condition is satisfied by all fast myelinated fibres in vertebrates: for a human motor fibre with $v = 70$ m/s, $L = 10$ mm, and $\tau_{AP} \approx 1$ ms, one obtains $L/v \approx 0.14$ ms, well below τ_{AP}. More precisely, the fraction of the action potential that elapsed at node N when node $N+1$ is activated is $\Delta t/\tau_{AP} \approx 0.14$, which means that $N+1$ is triggered during the earliest rising phase of the action potential at N – before any significant depolarisation has propagated axially. The 1949 anomaly is therefore not an exception but the general rule of saltatory conduction. The RC model is structurally incompatible with physiological conduction velocities across the entire class of fast myelinated fibres. In the IMH model, this is not a paradox: the periaxonal pressure wave arrives at $N+1$ independently of the electrical state of N, because the wave is the primary event and the electrical response is its consequence.

3.2. Hodgkin 1937: The Extrinsic Potential as Electromagnetic Shadow

Fifteen years before the HH equations were published, Hodgkin demonstrated that a nerve impulse blocked by cold or pressure produces, in the distal segment of the block, a transient potential that decreases exponentially with a space constant of approximately 2 mm [11]. He named it the *extrinsic potential* and showed that its spatial distribution is almost identical to that of an electrotonic potential applied artificially through external electrodes. He concluded that this local electric field was the cause of the increase in excitability observed beyond the block and offered this as a foundational support for an electrical theory of nervous transmission.

The IMH model accepts the experimental measurements without modification and proposes a different interpretation.

The cold or pressure block arrests the hydraulic wave in the periaxonal canal: mechanical compression triggers K^+ desorption from the gel sites and a pressure wave is initiated, but the elastic tube is interrupted and the wave cannot propagate further. What Hodgkin's silver-strip electrodes record beyond the block is the passive electrostatic field radiated by the arrested ionic desorption event, the electromagnetic shadow of a hydraulic wave that has been stopped. The exponential spatial decay with $L \approx 2\,\mathrm{mm}$ is precisely what the IMH model predicts for the passive spread of a charge

 doi:10.20944/preprints202603.0725.v6

perturbation in a cable-like conductor; it does not require and does not demonstrate that this passive spread is the *cause* of propagation in the unblocked fibre.

Three features of Hodgkin's own data are consistent with this reinterpretation. First, the extrinsic potential is *not propagated*: it declines monotonically with distance and carries no information forward, exactly as expected of a passive electrostatic field rather than an active transmission signal. Second, the near-identity of its spatial distribution with artificially applied electrotonus demonstrates only that the nerve cable conducts electrostatic fields passively, a property the IMH model does not contest. Third, the increase in excitability beyond the block, which Hodgkin attributes to local electric circuits, is equally explained in the IMH framework by sub-threshold mechanical compression transmitted through the periaxonal fluid immediately adjacent to the block face: partial gel deformation lowers the K^+ desorption threshold without initiating a full phase transition, reproducing the observed reduction in electrical threshold of 80–90%.

Hodgkin 1937 is therefore not evidence against the IMH model. It is the earliest recorded measurement of the electromagnetic shadow that the IMH framework predicts accompanies every hydraulic wave, blocked or propagating. That this shadow was interpreted as the cause of transmission, rather than its consequence, is the founding interpretive choice from which the HH model subsequently developed. The physical basis of this shadow is now quantitatively established: at hydrated biointerfaces, fluctuating electric fields generated by interfacial water and ion redistribution reach amplitudes of 13–25 MV/cm with a correlation time of 300 fs, originating predominantly from the first two water layers rather than from any transmembrane current [34]. The potential recorded by an external electrode is the electrostatic projection of a local ion redistribution event, not its cause.

3.3. The RC Invariance Argument

In classical cable theory, $\tau = R_{\text{axial}} \cdot C_{\text{membrane}}$. Both resistance and capacitance scale with internodal length L, as shown in equation (12), where ρ_i is axoplasm resistivity, r is axon radius, c_m is specific membrane capacitance and L is internodal length:

$$R_{\text{axial}} = \frac{\rho_i L}{\pi r^2}, \qquad C_{\text{membrane}} = c_m \cdot 2\pi r \cdot L \tag{12}$$

Equation (12) shows directly that $\tau = R_{\text{axial}} \cdot C_{\text{membrane}}$ scales as L^2: doubling the internodal length doubles resistance and doubles capacitance, quadrupling the time constant. The apparent velocity gain attributed to increased internodal spacing in myelinated fibres is therefore an arithmetic artefact: the RC reduction from lower capacitance per unit length is exactly cancelled by a proportional resistance increase. Myelination cannot accelerate conduction through the electrical mechanism alone. The hydraulic model does not require such cancellation: the velocity is determined directly by E_{myelin} through equations (3) and (4).

3.4. Thermal Signatures of the Action Potential

Ichiji Tasaki documented over six decades a series of observations incompatible with the purely electrical model: longitudinal mechanical displacement of the myelin sheath coincident with the action potential, near-zero net heat exchange and anomalous bidirectional conduction results [12]. These observations were noted and set aside by the field for lack of a theoretical framework capable of integrating them. The IMH model provides this framework: Tasaki's longitudinal myelin displacement is the macroscopic surface signature of the periaxonal pressure wave. His thermal measurements satisfy equation (5).

Masson and Gallot (2008) provided a more recent and quantitatively rigorous treatment of thermal exchange during the action potential [13], using a statistical physics model of ionic and water effusion through membrane nano-channels. Their model predicts a temperature variation of approximately 22 μK for a 10 μm radius axon, in good agreement with experimental measurements [12]. Crucially, Masson and Gallot identified coupled water flux as a necessary component of the thermal account—a conclusion that converges independently on the IMH framework. However, their model remains

 doi:10.20944/preprints202603.0725.v6

within the interpretive structure of the HH: the effusion is trans-membranous, the channels are the primary actors, and the near-zero net thermal balance expressed in equation (5) is not addressed. The IMH model proposes the missing constraint: the three-way coupling of lipid, gel, and water contributions is the physical reason why the net exchange approaches zero—not a coincidence to be quantified after the fact.

Terakawa [53] provided the corresponding direct measurement in the perfused squid giant axon: a transient change in intra-axonal hydrostatic pressure, coupled in time to the membrane potential, accompanying each action potential. The pressure transient is of the order of 1–10 mPa and coincides with the rising and falling phases of the depolarisation. A measurement of intra-axonal pressure variation coupled to the membrane potential is the direct hydraulic signature of the IMH phase transition: the electrical event and the pressure event are two projections of the same underlying ionic-hydraulic transition in the periaxonal gel. Terakawa's data were obtained in the same preparation used by Hodgkin and Huxley, with an established intracellular perfusion technique, and published in a mainstream physiology journal; they have not been integrated into any theoretical framework of nerve conduction in the forty years since. The IMH model reads them as what they directly are: a measurement of the pressure component of the hydraulic wave that the framework predicts.

3.5. The Cnidarian Nematocyst as Macroscopic Proof of Principle

The nematocyst of cnidarians demonstrates the ionic-hydraulic coupling mechanism on a directly measurable scale [14]. The organelle withstands an osmotic pressure of 150 bar, discharges in 700 ns, and produces an acceleration of 5.4×10^6 g. The trigger is Ca^{2+} desorption from a polyanionic capsule matrix, the same ionic-gel phase transition proposed for the periaxonal space in vertebrate axons, operating with measurable parameters. Cnidarians are among the first animals with a nervous system (>500 Myr), which established the ionic-hydraulic mechanism as evolutionarily ancient. The nematocyst is the bottom of the hydraulic fractal: the same principle operating at the nm– μm scale in 700 ns operates at the μ m scale in ms in the axon and at larger scales over longer time constants in the astrocytic syncytium and glymphatic system.

3.6. Axonal Mechanics: The Gel Identity of the Cytoskeleton

Independent biomechanical evidence for the gel nature of the interior of the axon was provided by Dubey et al. (2020), using a strain-controlled optical-fibre force apparatus in chick dorsal root ganglion axons [20]. The authors demonstrate three properties that are diagnostic of a polyelectrolyte gel rather than a simple viscous fluid or a microtubule cable: (i) the axon exhibits a *strain* softening response in which the steady-state elastic modulus decreases with increasing strain; (ii) the long-time behaviour is that of a *viscoelastic solid*, with a non-zero steady-state tension and memory of the initial state; (iii) the dominant mechanical contributor is not the microtubule bundle but the *actin-spectrin periodic lattice*, which buffers tension by reversible unfolding of the repeat domains of the spectrin.

These findings were obtained by researchers working entirely within the framework of biophysics and cytoskeletal mechanics, without reference to the HH model or nerve conduction. Their characterisation of the axonal cortex as a tension-buffering gel with solid-like long-time behaviour and strain-softening is precisely the material description required by the IMH model for the substrate that undergoes an ionic-hydraulic phase transition during the action potential. The convergence is independent and unintentional.

3.7. Matsumoto-Tasaki 1984: The Gel-Channel Coupling Demonstrated in the Native Preparation

The strongest experimental anchor for the mechanosensitive character of the nodal gate is provided, paradoxically, by the very preparation on which the HH model was built: the squid giant axon. Matsumoto, Ichikawa and Tasaki [51,52], working in Tokyo in the early 1980s, demonstrated that disruption of the axonal microtubule scaffold by colchicine applied intracellularly through the perfusion technique of Baker, Hodgkin, and Shaw abolishes the sodium current and, in a companion paper, the asymmetric displacement current (the gating current) of the voltage-clamped squid axon.

 doi:10.20944/preprints202603.0725.v6

Restoration was achieved by re-perfusion with purified microtubule proteins and a 260 kDa protein fraction, re-establishing both the sodium current and the gating current. Two consequences follow, both of them structural rather than quantitative, and both of them incompatible with the textbook reading of the HH model. First, the Nav channel conformational cycle is not an autonomous voltage-dependent property of the channel protein: it requires the intact microtubule-based cytoskeleton of the axon. Second, the gating current itself – the electrophysiological signature most commonly cited as direct evidence of the HH voltage-sensor mechanism – depends on the cytoskeleton, and therefore cannot be interpreted as a purely electrical property of an isolated channel protein. These results were obtained in situ, in the same preparation that Hodgkin and Huxley used, by investigators working explicitly within the HH tradition. They have not been cited in the mainstream channel literature that followed, and the heterologous-expression paradigm that became dominant after 1985 removed the cytoskeletal context in which the original measurements were made. The IMH model reads the Matsumoto-Tasaki result as a direct structural demonstration of the coupling between the nodal gel and the voltage-gated channel: the channel conformational cycle requires mechanical coupling to the cytoskeletal scaffold, because the opening is not primarily a response to voltage but to the mechanical state of the gel in which the channel is embedded. The HH preparation itself contains the evidence against the purely electrical reading of the HH mechanism.

4. Predictions

4.1. Myelin Elastic Modulus and Conduction Velocity

Prediction: Conduction velocity in myelinated axons correlates with the elastic modulus E_{myelin} of the myelin sheath (measurable by atomic force microscopy in isolated fibres), independently of the channel density Na^{+}.

The HH model predicts that the velocity is determined by the kinetics and density of the channels. The IMH model predicts that it is determined by myelin rigidity via equations (3)–(4). The two predictions are orthogonal and experimentally separable. Demyelinating conditions that reduce E_{myelin} should slow conduction in proportion to $\sqrt{E_{\text{myelin}}}$, not in proportion to channel loss.

4.2. Mechanoreceptor Adaptation as Hydraulic Geometry

Prediction: Altering the fluid volume or viscosity of sensory corpuscles (Pacinian, Meissner, Krause end bulbs) without modifying receptor channel composition should shift the adaptation rate and frequency selectivity according to hydraulic equilibration time calculations derived from equation (4).

In the HH framework, adaptation is a property of channel kinetics. In the IMH model, it is a property of the hydraulic geometry of the corpuscle. The two models make quantitatively different predictions for the same viscosity manipulation.

4.3. Terminal Arborisations: Slowness as Geometric Amplifier of the Umwelt

Sensory terminal arborisations are the finest and slowest branches of the peripheral nervous system. Within the HH framework, this slowness is a physical limitation of small-diameter unmyelinated fibres. Within the IMH model, it is an evolutionary calibration: the temporal bandwidth of biologically relevant events determines the hydraulic geometry of the terminal arbour.

A punctate mechanical stimulus activates multiple terminal branches at different distances from the integration point of the arborisation, irrespective of fibre type. The resulting delays in arrival between branches encode the spatial geometry of the stimulus as a temporal signature, as expressed in equation (13), where L_i and L_j are the lengths of two terminal branches reaching the same receptive field point through different paths, and v_{terminal} is the hydraulic wave velocity in those branches:

$$\Delta t_{ij} = \frac{L_i - L_j}{v_{\text{terminal}}} \tag{13}$$

 doi:10.20944/preprints202603.0725.v6

Equation (13) establishes the fundamental encoding principle: Δt_{ij} is the temporal delay between the two hydraulic messages reaching the integration point of the arborisation from the same stimulus point. This delay is a spatial coordinate transformed into a temporal one. *Slowness amplifies geometry.*

The motor arborisation inverts the principle: synchrony of muscle fibre contraction requires synchrony of hydraulic wave arrival at motor end-plates. Equal branch lengths produce simultaneous arrival and maximal impulsive force; unequal branch lengths produce staggered arrivals and temporally distributed force.

Falsifiable prediction: The spatial resolution of a cutaneous receptor field correlates with the maximum branch length differential of its sensory arborisation, measurable by anatomical reconstruction. For motor units: the temporal profile of the compound EMG reflects terminal branch length distribution, distinguishable from predictions based on fibre conduction velocity alone.

4.4. Motor Tremor as Hydraulic Interference

Smooth motor fusion requires successive hydraulic waves to arrive at terminal arborisations in constructive temporal superposition. The critical firing frequency above which destructive interference produces tremor is given by equation (14), where $v_{\text{hydraulic}}$ is the hydraulic wave velocity in the terminal branches and $L_{\text{max branch}}$ is the length of the longest branch in the motor arborisation:

$$f_{\text{critical}} = \frac{v_{\text{hydraulic}}}{L_{\text{max branch}}} \tag{14}$$

Equation (14) provides a direct geometric interpretation of pathological tremor: if the firing frequency exceeds f_{critical}, successive hydraulic wavefronts arrive at terminal end-plates before the preceding wave has fully dissipated, producing destructive superposition and loss of smooth force summation. The three types of clinical tremor –Parkinsonian (4–6 Hz), essential (8–12 Hz), cerebellar (variable)—correspond to three distinct hydraulic regimes, each with a characteristic branch length distribution.

4.5. Composite Temporal Decoding and the Libet Latency

The peripheral nerve fibres span a conduction velocity range of 0.5–120 m/s. On a path length of 1 m, arrival delays range from 10 ms (Aα) to 1000 ms (C fibres). The Libet threshold of approximately 500 ms for conscious sensory perception is, in the IMH model, the minimum temporal integration window required to receive and decode the complete composite message, including its slow affective C-fibre component [17].

Prediction: Selective pharmacological blockade of C-fibre hydraulic transmission should abolish the subjective feel quality of a stimulus while preserving its fast discriminative component. Disruption of astrocytic gap junctions should selectively alter C-fibre signal integration while preserving fast-fibre processing [17].

4.6. Electrical Stimulation as Gel Trigger

The apparent success of external electrical field stimulation has been cited as evidence against purely mechanical models of nerve conduction. In the IMH model, this objection is resolved by the polyelectrolyte gel. An external electric field acts directly on the charged gel matrix and adsorbed ions, triggering the desorption electrically rather than mechanically. The same ionic-hydraulic phase transition is initiated; only the triggering stimulus differs.

Prediction: The threshold electric field for nerve stimulation correlates with the gel adsorption affinity constants (Hofmeister series position of the dominant adsorbed cation), not only with the membrane capacitance. This can be tested with gel-modifying agents that shift the adsorption affinity without altering the membrane electrical properties.

 doi:10.20944/preprints202603.0725.v6

4.7. Non-Contamination Between Adjacent Fibres

Adjacent axons in a nerve bundle transmit distinct signals simultaneously without crosstalk. In the HH framework, the isolation is provided by myelin insulation. In the IMH model, each fibre is a sealed periaxonal canal; hydraulic waves cannot propagate between structurally independent tubes.

Prediction: Selective mechanical disruption of the periaxonal seal between two adjacent fibres—without affecting their electrical insulation—should produce hydraulic crosstalk detectable as correlated mechanical signals in both fibres simultaneously.

4.8. Electromagnetic Dipole Geometry

A propagating hydraulic wavefront generates a moving ion desorption–adsorption dipole along the axon, producing a propagating electromagnetic dipole rather than a stationary monopole.

Prediction: High-resolution EEG/MEG source modelling of single-fibre or small-fascicle signals should detect a dipolar electromagnetic signature progressing at hydraulic velocity, quantitatively distinguishable from the monopolar source geometry predicted by HH.

4.9. Axon Diameter Limits: Three Coupled Constraints

The IMH model predicts a set of coupled physical limits on axon diameter that jointly explain an otherwise unaccounted observation: large-diameter unmyelinated fibres do not exist in nature.

4.9.1. The Refractory Constraint in Unmyelinated Fibres

In the IMH model, the refractory zone is the length of the axon occupied by a propagating hydraulic wave that is still undergoing K^+ adsorption at gel sites. As the diameter of the axon increases, the length of the refractory zone increases with it (it scales as $L_{\text{active}} \propto d$; see Section 4.9.3 for the distinct scaling laws of amplitude and velocity). The critical constraint is not on a single action potential but on the following one: successive impulses must not enter the refractory zone of the preceding wave. The maximum firing frequency is therefore inversely proportional to refractory zone length and, by extension, to axon diameter:

$$f_{\max} \propto \frac{1}{d} \tag{15}$$

where d is the diameter of the axon. A large-diameter unmyelinated fibre would be structurally limited to very low firing frequencies, rendering it functionally useless for information transmission at the signal bandwidths required by vertebrate nervous systems. The HH model does not offer a principled reason why large unmyelinated fibres should not exist; the IMH model predicts their absence from the energy and information-theoretic first principles.

4.9.2. The Ion Density Constraint

Maintaining a sufficient safety factor for hydraulic wave propagation requires a minimum density of adsorption sites (and, therefore, ion channels as secondary electromagnetic reporters) per unit of membrane area. As diameter increases, the gel volume and ion reservoir available per unit surface scale differently, eventually requiring a channel density that is metabolically and structurally untenable. This is the same constraint identified at the nanoscale in the companion paper [24]: the ionic reservoir is finite and scales unfavourably with the diameter for unmyelinated fibres.

 doi:10.20944/preprints202603.0725.v6

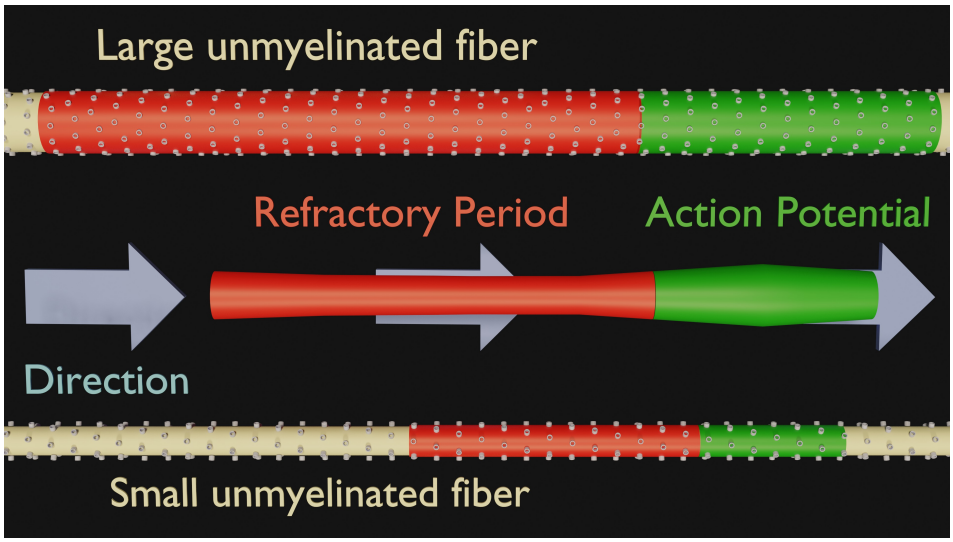

Figure 2. Refractory constraint and ion density as a function of axonal diameter in unmyelinated fibres. The propagating action potential (green) is followed by a refractory zone (red) in which K^+ adsorption onto gel sites is still in progress and a second impulse cannot be sustained. *Top*: In a large-diameter unmyelinated fibre, the refractory zone occupies a proportionally greater length of the axon, severely limiting the maximum firing frequency ($f_{max} \propto 1/d$, equation 15); simultaneously, the gel volume scales as d^2 while the adsorption site density per unit surface area scales unfavourably, imposing the ion density constraint of Section 4.9.2. *Bottom*: In a small-diameter unmyelinated fibre, both constraints are satisfied: the refractory zone is short relative to axon length and the ion reservoir per unit surface remains adequate. The IMH model predicts that beyond a critical diameter ($d \approx 1.5\,\mu$m), large unmyelinated fibres become simultaneously frequency-limited and ionically inviable—explaining their absence from vertebrate nervous systems on physical, not developmental, grounds. The schematic also illustrates the proportionality between wave amplitude and fibre diameter: the hydraulic wavefront in the large fibre (centre) is broader and more energetically costly, imposing the amplitude–velocity trade-off discussed in Section 4.9.3.

4.9.3. The Amplitude-Velocity Trade-Off and the Engineering Parallel

The biological constraint stands in instructive contrast to digital electronics. In semiconductor technology, the voltage amplitude has been systematically reduced – from 5 V in early microprocessors to below 1 V in modern architectures—because a lower amplitude enables faster switching: less charge to move, lower RC time constant, higher clock frequency. The nerve fibre faces the inverse constraint. In the IMH model, a larger amplitude hydraulic wave (requiring more ionic desorption, more channel activity, and more energy) is required to propagate faster or over a larger diameter. Biology cannot "lower the voltage" without losing propagation. This asymmetry defines a hard architectural ceiling on unmyelinated conduction speed.

4.9.4. Myelination as the Evolutionary Solution

The three above constraints converge on the same conclusion: beyond a critical diameter, unmyelinated fibres become simultaneously frequency-limited, energy-inviable, and amplitude-constrained. Myelination resolves all three by confining the hydraulic wave to the periaxonal canal at the Ranvier node, where the relevant geometry is the diameter and length of the node –not the full diameter of the internode. The node can be small while the internode is large, decoupling the amplitude requirement from the velocity requirement.

For myelinated fibres, two further constraints apply. First, the node length sets a minimum below which the ionic desorption event cannot sustain a self-propagating wave. Second, increasing the diameter of the fibre requires proportionally longer internodes to preserve the hydraulic impedance match at the node, imposing a geometric scaling law between the length of the internode, the geometry of the node and the thickness of the myelin.

 doi:10.20944/preprints202603.0725.v6

Prediction: The upper diameter limit of unmyelinated fibres and the node-to-internode geometry of myelinated fibres should follow quantitative scaling laws derivable from equations (3)–(4) and the ion adsorption isotherm (2). Specifically: (i) the diameter of the unmyelinated fibre should be bounded by a critical value above which f_{max} falls below the minimum physiological firing rate of the fibre class; (ii) in myelinated fibres, the ratio of node length to internode length should correspond to the elastic modulus in the manner prescribed by equation (4).

4.9.5. The Active Surface as the Unifying Variable

The arguments developed in the preceding sections can be unified by a single geometric quantity: the *active surface* $A_{\text{active}} = 2\pi r L_{\text{active}}$, defined as the lateral membrane area over which ionic desorption occurs during the propagating hydraulic event. For unmyelinated fibres, L_{active} is the length of the hydraulic wavefront along the axon; for myelinated fibres, it is the length of the Ranvier node. In both cases, A_{active} determines the total number of K^+ ions desorbed per wave cycle and, therefore, the amplitude of the hydraulic pressure pulse.

For unmyelinated fibres, $L_{\text{active}} \propto r$ (the wavefront length scales with diameter because the wave is geometrically self-similar), so:

$$A_{\text{active}}^{\text{unmyel}} = 2\pi r \cdot L_{\text{active}} \propto r^2 \propto d^2 \tag{16}$$

Both amplitude and conduction velocity increase with d, but not at the same rate: amplitude $\propto d^2$ (from A_{active}), while velocity $\propto d^{1/2}$ from the Moens–Korteweg equation for an elastic tube without confining myelin, yielding an amplitude-to-velocity ratio $\propto d^2/d^{1/2} = d^{3/2}$ that constitutes the energetic ceiling identified above: the energy cost per unit of conduction velocity increases as $d^{3/2}$, making arbitrarily large unmyelinated fibres thermodynamically inviable.

For myelinated fibres, empirical data show that the node length L_{node} is *independent of the diameter* of the axon [31]: regression of the node length against the node diameter yields a slope not significantly different from zero across a 4-to-8-fold range of node lengths. Therefore:

$$A_{\text{active}}^{\text{myel}} = 2\pi r \cdot L_{\text{node}} \propto r \propto d \tag{17}$$

The active surface of the node scales linearly with diameter, and so does the amplitude of the hydraulic pulse generated at each node. Since the conduction velocity also scales as $v \propto d$ in myelinated fibres (see Section 4.9.6 below), the amplitude-to-velocity ratio is *constant* throughout the full diameter range of myelinated fibres.

$$\frac{A_{\text{active}}^{\text{myel}}}{v} \propto \frac{2\pi r \cdot L_{\text{node}}}{d} = \frac{\pi d \cdot L_{\text{node}}}{d} = \pi L_{\text{node}} = \text{const} \tag{18}$$

This constancy is not an accident of design: it is the geometric consequence of confining the active surface to the node, whose length is a free parameter decoupled from diameter. Myelination achieves what unmyelinated architecture cannot achieve – a constant energetic cost per unit of conduction velocity – by separating the two degrees of freedom (r and L_{node}) that jointly determine A_{active}.

A further consequence follows directly. Because L_{node} is independent of diameter but nonetheless varies substantially between axons (up to 8 times in cortical axons [31]), it constitutes a *plastic tuning parameter* for conduction velocity that operates independently of myelination thickness and internode length. In the IMH framework, this plasticity is the geometric mechanism by which the nervous system adjusts hydraulic wave amplitude, and therefore signal arrival time, on a fibre-by-fibre basis without altering the axon calibre. The HH model offers no mechanistic account of why node length should influence conduction speed: in a purely electrical framework, a longer node simply exposes more membrane capacitance, which should *slow* conduction by increasing the charge required to depolarise the downstream node. The IMH model predicts the opposite: a longer node generates a larger hydraulic pressure pulse, which arrives at the next node sooner. The empirical observation that

 doi:10.20944/preprints202603.0725.v6

longer nodes conduct faster [31] is a direct falsification of the HH prediction and a direct confirmation of the IMH prediction.

Falsifiable prediction (P_α): the increase in conduction velocity per unit increase in node length should be quantitatively predictable from the Moens–Korteweg equation and the gel adsorption isotherm, without free parameters. Specifically, $\Delta v/\Delta L_{\text{node}} = (2\pi r/A_{\text{ref}}) \cdot \partial v/\partial A_{\text{active}}$, where A_{ref} is the active reference surface and $\partial v/\partial A_{\text{active}}$ is derived from equation (3). This relation can be tested by simultaneous measurement of the length of the node and the single-fibre conduction velocity in identified axons of known diameter.

The projection of A_{active} onto the propagation axis introduces another constraint that distinguishes myelinated architecture from unmyelinated architecture. In unmyelinated fibres, the desorption event unfolds continuously along L_{active}: every surface element dA contributes to the advancing wavefront, and the temporal unfolding of the action potential – the absolute refractory period during desorption, the relative refractory period during adsorption – is encoded directly in L_{active}. In myelinated fibres, A_{active} is concentrated at the node over a short L_{node}: the hydraulic pulse is quasi-instantaneous and quasi-punctual, and its projection onto the propagation axis produces a high-amplitude impulsion that traverses the internode Λ before dissipating. The temporal information lost at the node is re-encoded at a higher level in the internodal transit time Λ/v.

This geometric distinction implies a critical constraint on L_{node}. As L_{node} increases toward Λ, the node progressively loses its punctual character: the desorption event spreads axially, the hydraulic pulse loses its impulsive concentration, and the projection onto v decreases. At the limit $L_{\text{node}} \to \Lambda$, the fibre becomes functionally equivalent to a large unmyelinated fibre and encounters the three constraints identified above – the energetic ceiling, the refractory constraint, and the ion density constraint. Below a minimum $L_{\text{node}}^{\min}$, the active surface is insufficient to generate a pulse capable of traversing the internode: the wave becomes stationary. The conduction velocity is therefore a *bell-shaped function* of L_{node} at constant diameter and internode length:

$$\begin{aligned} v(L_{\text{node}}) \text{ is maximal at } L_{\text{node}}^{\text{opt}} &\ll \Lambda, \\ v \to 0 \text{ for } L_{\text{node}} &\lesssim L_{\text{node}}^{\min} \text{ and } L_{\text{node}} \gtrsim \Lambda \end{aligned} \tag{19}$$

The descending branch of this function – where the conduction velocity decreases as L_{node} increases beyond $L_{\text{node}}^{\text{opt}}$ – has never been experimentally sought, because the HH model predicts no such optimum: in a purely electrical framework, the length of the node affects only the membrane capacitance, and the relationship between the length of the node and the conduction velocity is monotone. The IMH model predicts a non-monotone relationship with a well-defined optimum determined by the ratio L_{node}/Λ and the hydraulic impedance of the internode.

Falsifiable prediction (P_β): In myelinated axons of fixed diameter and fixed internode length, conduction velocity as a function of node length should follow a bell-shaped curve with a maximum at $L_{\text{node}}^{\text{opt}}$, and should decrease – eventually reaching a stationary wave condition – for node lengths approaching Λ. This prediction is testable by combining the node length manipulation methodology of Arancibia-Cárcamo et al. [31] with single-fibre conduction velocity measurement throughout the observed range of node lengths, including the longest nodes currently documented.

Involuntary experimental support for the descending branch is provided by pathological observations reviewed by Arancibia-Cárcamo and Attwell (2014) [32]. In multiple sclerosis, spinal cord injury, cerebral hypoperfusion, ageing, and glutamate excitotoxicity, the Ranvier node undergoes lengthening, an increase in L_{node} beyond its physiological value, accompanied by redistribution of Kv1 channels from the juxtaparanode toward the node and paranode, and by a reduction in conduction velocity or conduction failure. In the HH framework, the lengthening of the nodes slows conduction because it increases the capacitance of the nodes, requiring more charge from the Nav channels to depolarise the next node – an explanation that predicts a monotonous relationship between L_{node} and conduction slowing. In the IMH framework, the lengthening of the node moves L_{node} beyond

 doi:10.20944/preprints202603.0725.v6

$L_{\text{node}}^{\text{opt}}$ to the descending branch of the bell-shaped curve: the hydraulic pulse loses its impulsive concentration, the osmotic amplification by the Nav channels becomes spatially dispersed, and the wave amplitude at the next node falls below the desorption threshold. The two frameworks make the same qualitative prediction for the direction of the effect but differ in their mechanistic account and in their quantitative predictions: the HH framework predicts a monotone slowing proportional to the added capacitance, while the IMH framework predicts an accelerating decline as L_{node} approaches Λ, with a sharp transition to the conduction block. The redistribution of Kv channels observed in these pathologies is, in the IMH framework, a secondary consequence of loss of integrity of the osmotic cycle rather than a primary cause of conduction failure.

4.9.6. Quantitative Velocity-Diameter Scaling and the Collapse Exponent

The three constraints above generate a characteristic velocity-diameter profile whose shape is quantitatively derivable from equations (3)–(4). Within the biologically viable range, myelinated fibres follow the empirically established linear relation $v \propto d$ [25,26]. This linearity is a direct consequence of the Moens-Korteweg equation under the anatomical constraint that myelin thickness scales proportionally with the diameter of the fibre (ratio $g \approx 0.6$, constant across the fibre classes [27]): since $h \propto d$ and the elastic modulus of a laminated cylindrical shell scales as $E_{\text{myelin}} \propto d^2$, equations (3) – (4) yield $v \propto d^1$ exactly. The parabolic relation $v \propto d^{1/2}$ predicted by cable theory [27] and empirically validated only by extrapolation to the giant squid axon, a composite fusion of hundreds of smaller axons [5] whose hydraulic architecture is uncharacterised, is not a prediction of the IMH model.

Beyond the anatomical limits ($d_{\max} \approx 20\,\mu$m for myelinated fibres; $d_{\max} \approx 1.5\,\mu$m for unmyelinated fibres), the IMH model predicts that effective conduction velocity does not continue to increase but collapses, following a power law with exponent $-3/2$:

$$v_{\text{eff}}(d) = v_{\max}\left(\frac{d_{\max}}{d}\right)^{3/2}, \quad d > d_{\max} \tag{20}$$

The exponent $3/2$ is not fitted but is derived from two independent physical contributions that combine multiplicatively. For myelinated fibres beyond $d_{\max}$: (i) the cost of ionic desorption scales as d^2 (gel volume), while (ii) the hydraulic driving pressure scales as d^{-1} by the Laplace relation $\Delta P = 2\gamma/r$; therefore, the ratio of available energy to required pressure decreases as d^{-3}, and since the velocity scales as the square root of this ratio in the Moens-Korteweg framework, the effective velocity declines as $d^{-3/2}$. For unmyelinated fibres beyond $d_{\max}$: without a confining myelin sheath, the hydraulic wave radiates cylindrically; the amplitude of a cylindrical wave decays as $r^{-1/2}$, and the wave can no longer sustain propagation when the amplitude falls below the gel desorption threshold. The combined effect of amplitude decay and increased gel volume again yields an effective velocity that decreases as $d^{-3/2}$.

The lower end of the myelinated range is provided by Waxman and Bennett [25], who demonstrated that in the central nervous system, myelinated fibres with diameters as small as $0.2\,\mu$m conduct faster than unmyelinated fibres of the same diameter–directly contradicting the Rushton critical-diameter argument (which predicts that myelination ceases to accelerate conduction below $\sim 1\,\mu$m) and confirming the linear relation $v \propto d$ at the small-diameter end. Within the IMH framework, this observation is explained by the noise properties of the CNS environment: the periaxonal space is hydraulically better confined (blood-brain barrier, glial envelope, cerebrospinal fluid cushion) than the peripheral nerve, so the minimum wave amplitude required for reliable propagation is lower, and the linear regime extends to smaller diameters. The minimum myelinated fibre diameter is not a universal constant, but an environmental noise floor.

 doi:10.20944/preprints202603.0725.v6

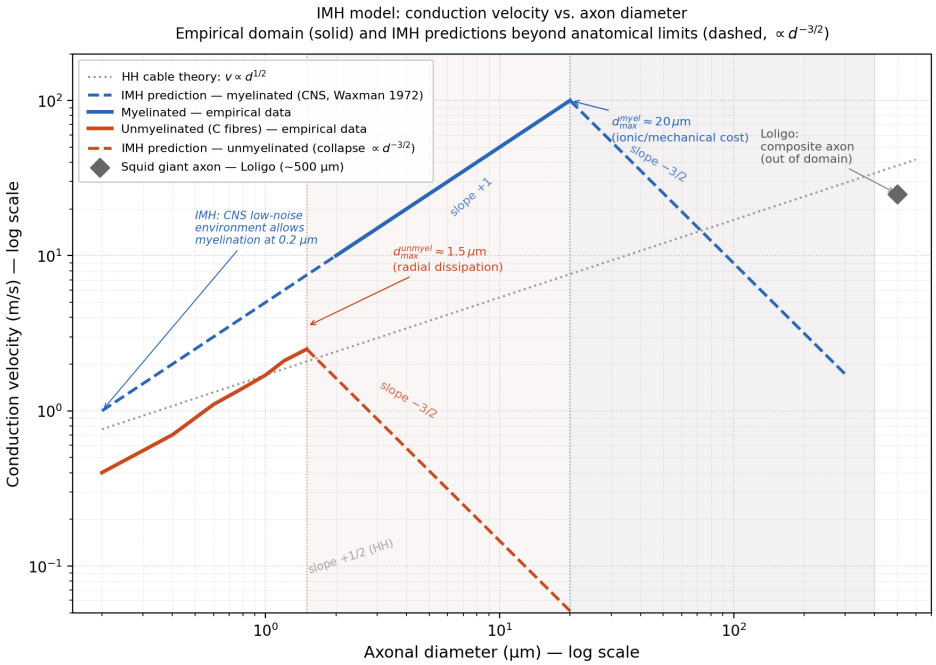

Figure 3. Conduction velocity as a function of axonal diameter: empirical data and IMH predictions (log–log scale). Solid lines show the empirically established velocity–diameter relations for myelinated fibres (blue, Hursh 1939; Waxman and Bennett 1972 [25]) and unmyelinated C fibres (red). Dashed lines extend each relation beyond the respective anatomical limits ($d_{\max}^{\text{myel}} \approx 20\,\mu$m; $d_{\max}^{\text{unmyel}} \approx 1.5\,\mu$m) according to the IMH collapse law (equation 20, exponent $-3/2$, derived from Moens–Korteweg mechanics). In log–log coordinates, the empirical linear relation $v \propto d^1$ (slope $+1$, blue solid) is a straight line, as is the collapse ($v \propto d^{-3/2}$, slope $-3/2$, blue and red dashed). The dotted grey line shows the Hodgkin–Huxley cable-theory prediction $v \propto d^{1/2}$ (slope $+1/2$, Rushton 1951), which continues to rise without bound and predicts conduction in arbitrarily large unmyelinated fibres—a prediction contradicted by anatomy. The diamond marker indicates the squid giant axon (*Loligo*, $d \approx 500\,\mu$m, $v \approx 25\,$m/s), which lies far outside the biological domain of individual axons and whose inclusion by Rushton to validate the $v \propto d^{1/2}$ relation is critiqued in Section 4.9.6. The two models diverge maximally in the zone 2–50 μm for unmyelinated fibres, where the IMH predicts collapse and HH predicts continued acceleration—a range directly accessible to experiment.

4.10. Cumulative Nodal Surface: The Geometry of the Active Wavefront

A consequence of the analysis of L_{active} and L_{node} developed above is directly testable by a simple counting argument that to our knowledge has never been made explicit in the myelin literature. For a human motor axon conducting at $v \approx 100$ m/s with an internode length $\Lambda \approx 1$ mm and a pulse duration $\Delta t \approx 1$ ms, the total active length of the wave at any instant is $\Delta x = v \cdot \Delta t = 100$ mm. This active length contains approximately $N_{\text{node}} \approx \Delta x / \Lambda \approx 100$ Ranvier nodes simultaneously engaged in the ionic-hydraulic cycle. Each node has a length L_{node} of order 1 μm and a circumference $2\pi r$ of order a few micrometres, giving a total electrically active surface per node of approximately 1–10 μm^2. The cumulative active surface across the wave is therefore $A_{\text{cumulative}} \approx N_{\text{node}} \cdot 2\pi r \cdot L_{\text{node}} \approx 10^2$–$10^3$ μm^2, which is of the same order as the continuous active surface of an unmyelinated axon of equivalent L_{active} and calibre. The myelinated fibre, considered at the scale of the propagating wave rather than at the scale of the individual node, is not a low-surface architecture. It is a discretised architecture, in which the same total active surface is concentrated at discrete points spaced by Λ, with hydraulic transit between them.

The following two implications are given. First, the argument frequently made in favour of the saltatory model that myelination economises membrane surface and, therefore, energy is quantitatively incorrect at the scale of the wave: the cumulative active surface is not reduced; it is redistributed. The saving is not in surface but in internodal transit, which is a hydraulic transit through an elastic tube and not a membrane depolarisation event. Second, the IMH model does not need to postulate a special

 doi:10.20944/preprints202603.0725.v6

large active surface at the node: the measured dimensions of the node, summed over the $N_{\text{node}} \approx 100$ simultaneously active nodes, are quantitatively sufficient to generate the observed action potential. The prediction is that the pressure pulse generated at each node, integrated in N_{node}, should match the transient pressure measured intra-axonally by Terakawa [53].

Falsifiable prediction ($\mathbf{P}_\gamma$): for a myelinated axon of known Λ, L_{node}, r, Δt and v, the transient measured intra-axonal pressure should match, to within a factor of order unity, the cumulative Moens-Korteweg pressure generated by the $N_{\text{node}} = v \cdot \Delta t / \Lambda$ simultaneously active nodes. The HH framework does not make such a prediction because it invokes no hydraulic wave; the IMH framework does, however, make it directly, with no free parameters once the gel adsorption isotherm is fixed.

5. Evolutionary Perspective

The gel generating hydraulic pressure in a confined space operates recursively across at least five biological scales: nematocyst (nm–μm, ns) [14], periaxonal axonal space (μm, ms), dendritic arborisations (mm, tens of ms), astrocytic syncytium (cm, s) and glymphatic system (organ, circadian). The fractal geometry of neural arbours, from terminal arborisations to dendritic trees to cortical columns, may be the spatial imprint of this temporal recursion.

The Heimburg-Jackson soliton model [9] converges to the IMH framework from membrane thermodynamics: both models require reversible mechanical wave propagation and near-zero net heat exchange. The two frameworks are complementary, addressing different physical levels of the same phenomenon.

The soliton theory and the coupled-wave ensemble model share a structural difficulty that neither framework has resolved. The spatial extension of the action potential, the length of membrane simultaneously in its active state, is given by $\Delta x = v \cdot \Delta t$ [35]: for a human motor neuron with conduction velocity 100 m/s and pulse duration 4 ms, $\Delta x = 40$ cm; for a hippocampal pyramidal neuron with velocity 2 m/s and duration 3.5 ms, $\Delta x = 7$ mm, while the neuron itself measures approximately 850 μm [35]. A wave that is eight times longer than the substrate in which it is supposed to propagate cannot be sustained by that substrate in any continuous-medium wave theory. The Heimburg-Jackson soliton, being a travelling density wave in the lipid bilayer, requires a continuous membrane substrate of length at least equal to its own spatial extension. The Engelbrecht coupled-wave ensemble [21], which superimposes three waves of different velocities and characteristic lengths, faces the same constraint compounded: the slowest wave, whose length sets the scale of the ensemble, cannot fit within a neuron shorter than itself.

The IMH model is not subject to this constraint. In the IMH framework, Δx corresponds to the active surface length L_{active} introduced in Section 4 – the axial extent of the desorption front at a given instant, not the length of a physical structure that must pre-exist along the axon. In myelinated fibres this front is further reduced to the node length $L_{\text{node}} \ll \Delta x$, and the wave is relayed node by node. A neuron shorter than Δx transmits the IMH wave without contradiction because the wave does not reside in the neuron – it traverses it.

Damasio's identification of C fibres as the primary substrate of felt experience [17] provides an independent clinical convergence: the slow peripheral hydraulic message arriving last is the affective dimension of perception, not noise. Descartes attributed neural function to hydraulic spirits; Damasio rediscovered the role of slow peripheral signals through clinical observation; the IMH model provides the biophysical substrate.

6. Discussion

The IMH model does not falsify the HH equations. It explains them. The HH model accurately describes the electrical correlates of the action potential in a preparation that has removed the gel, the periaxonal space, the Schwann cell, and mechanical coupling from the measurement. In those conditions, the electrical description is correct and complete. The IMH claim is that these conditions

 doi:10.20944/preprints202603.0725.v6

do not describe physiological nerve conduction and that the physical process in the intact fibre has a hydraulic primary layer that the HH electrical measurements capture only as a projection.

A further limitation of the HH preparation concerns the site of stimulation. In the HH voltage-clamp protocol, a section of isolated axon is stimulated at an arbitrary point along its length, a site that has no physiological counterpart. Nerve conduction in the intact organism is initiated at one of two geometrically specialised locations: the axon initial segment (AIS), where the density of the Nav channel is maximal, the intracellular gel reservoir is at its largest, and the geometry is optimised to initiate the ionic phase transition; or the fine terminal arborisations of the sensory fibres, where the active surface $A_{\text{active}} = 2\pi rL$ is minimal and the hydraulic wave self-amplifies progressively as it propagates towards larger-diameter branches. In both cases, the IMH model provides a natural account of threshold, directionality, and wave initiation that the HH model cannot offer, because HH was calibrated on a preparation that eliminates both initiation sites by design.

A unifying principle underlies the entire ionic architecture of the IMH model: the axonal membrane is not the seat of conduction but the boundary between two osmotic reservoirs whose asymmetry is the energy source of the hydraulic wave. Nature does not design; it exploits what exists on each side of every boundary. K^+ is the dominant intracellular cation, adsorbed at gel sites, available as the primary trigger of the phase transition. Na^+ is the dominant extracellular cation, free in solution at 145 mM, available as the osmotic amplifier of the wave. Extracellular K^+ released by Kv channels closes the cycle on the outside. The Donnan asymmetry that HH treats as a static boundary condition is, in the IMH framework, the thermodynamic engine of propagation. This asymmetry was not engineered; it is the equilibrium state of a polyelectrolyte gel in contact with a saline medium, and the nervous system propagates signals by periodically and locally disturbing it.

A direct consequence of this architecture is the near-universal constancy of spike duration across fibre types. In the HH framework, the duration of the spike is determined by the kinetic parameters of Nav and Kv gating, parameters fitted to the experimental data without a physical account of why they should be conserved. In the IMH framework, the duration of the spike is the period of the osmotic cycle: K^+ desorption of the gel, Na^+ influx through Nav, K^+ efflux through Kv, K^+ adsorption onto the gel. This cycle is governed by the adsorption/desorption kinetics of the polyelectrolyte gel and the geometry of the periaxonal canal, material properties that are quasi-invariant across fibre types of the same class, because the material is the same. The constancy of spike duration is therefore not a coincidence to be fitted: it is the constancy of the natural period of a physical oscillator whose restoring force is the thermodynamic drive toward gel equilibrium. The period of a pendulum is fixed by its length and gravity, rather than by the details of how it was set in motion, and the duration of the action potential is fixed by the kinetics of the gel cycle, rather than by the amplitude or geometry of the triggering stimulus.

Rvachev (2010) proposed an axoplasmic pressure wave model in which the propagating action potential is accompanied by a pressure pulse travelling along the axoplasm, stretch-modulating voltage-gated Na^+ channels and thereby accelerating their activation and inactivation beyond the rates predicted by purely electrical gating [18]. The Rvachev model identified the mechanical wave as a genuine component of propagation and proposed a concrete electromechanical coupling mechanism that anticipates the role of osmotic amplification assigned to Nav channels in Section 2 of the present work. However, it did not anchor the pressure wave in a substrate specified thermodynamically: the origin of the pressure pulse was discussed in terms of several possible drivers (actomyosin contractility, voltage-induced membrane movement, Ca^{2+} influx) without committing to a gel phase transition as the primary ionic event. The IMH model provides this anchor through the Ling-Tamagawa polyelectrolyte gel framework: the pressure wave is not merely an accompaniment, but the signature of a K^+ desorption event from the cytoplasmic gel, and the modulation of the stretch of the Nav channels becomes the mechanical trigger of an osmotic amplification step whose thermodynamic driving force is the Donnan asymmetry of the gel system.

 doi:10.20944/preprints202603.0725.v6

Barz et al. (2013) proposed a purely mechanical pressure-wave model in which ion channels are pressure-gated rather than voltage-gated [19]. That model correctly identified the wave as primary but lacked ionic-gel coupling: it had no threshold mechanism, no sigmoid, no ionic selectivity, and no account of electrical stimulation. The IMH model provides the missing components through the Ling-Tamagawa polyelectrolyte gel framework. The elementary molecular mechanism by which a single membrane protein converts ion binding energy into hydraulic work is formalised in a companion paper [33], which proposes the V→U membrane actuator as the evolutionarily ancestral motor underlying the ionic-hydraulic phase transition and identifies Ca^{2+} as the orchestrator of the reset cycle that defines both the absolute and relative refractory periods.

The need for such an extension is recognised within mainstream modelling, as noted in the Introduction. The theoretical positioning of the present model within the broader landscape of non-HH frameworks is clarified by Drukarch and Wilhelmus (2023), who distinguish two approaches to the multi-physics of the nerve signal: a bottom-up mechanistic approach that retains HH as the driving layer and adds mechanical coupling as an epiphenomenon, and a top-down thermodynamic approach that treats the nerve signal as emerging from the collective physics-chemical properties of the axolemma-ectoplasm complex [23]. The IMH model belongs unambiguously to the second category. Drukarch and Wilhelmus, moreover, provide an extensive treatment of Tasaki's gel phase transition framework – the bistable Ca^{2+}/Na^{+} ectoplasmic gel, volume phase transition, cooperative ion exchange, and refractory period as re-compaction kinetics – which constitutes the direct conceptual precursor of the ionic-gel layer of the present model. Their conclusion, that neuroscience "**should welcome and be open to different perspectives on modelling and explanatory understanding of the physics of the nerve signal,**" applies directly to the present work, and their publication in a mainstream peer-reviewed venue signals that this openness is no longer confined to the margins of the field.

Independent philosophical support for this positioning is provided by Carrillo (2024), whose survey of models of the nerve impulse in the *Routledge Handbook of Philosophy of Scientific Modeling* explicitly frames the contrast between the Hodgkin–Huxley model and thermodynamic alternatives in terms of Einstein's distinction between constructive (bottom-up) and first-principle (top-down) theories [22]. Carrillo notes that "**very little philosophical discussion has appeared**" on the implications of this controversy—a lacuna that the present work addresses from the mechanistic side. Notably, Carrillo's survey covers Tasaki's macromolecular model and the Heimburg–Jackson soliton framework but does not include the polyelectrolyte gel layer (Ling–Tamagawa–Matveev), which constitutes the ionic substrate common to both. The absence of this framework from the philosophical literature reflects its marginalisation within mainstream electrophysiology rather than any evidence deficiency and points to a gap that the IMH model is positioned to fill.

An additional convergence deserves explicit recognition. Manoj and Jaeken (2023), proposing the murburn concept as a unifying framework for cellular bioenergetics, situate Ling's association-induction hypothesis as a foundational precursor shared by several non-classical schools, and cite Tamagawa and Matveev directly as contemporary representatives of this tradition [28]. Tamagawa is himself a co-author of two murburn electrophysiology papers, one providing a critical comparative analysis of the membrane-pump and association-induction frameworks [29], and one repositioning Na^{+} / K^{+}-ATPase as a thermodynamic equilibrium facilitator rather than an active electrogenic pump [30]—a conclusion that directly corroborates the regulatory, non-primary role assigned to the pump in Section 2.1 of the present work. The murburn framework, centred on diffusible reactive species (DRS) as primary agents of ATP synthesis and cellular coherence, addresses the bioenergetic layer that the present model does not treat explicitly. The two frameworks are complementary rather than competing: the IMH model describes the propagation physics of the nerve signal, while the murburn framework addresses the metabolic resetting that restores the gel to its adsorption-competent state between impulses. In this reading, the refractory period acquires a biochemical correlate, DRS–mediated gel recompaction, that is absent from both HH and purely mechanical wave models. Ling's

 doi:10.20944/preprints202603.0725.v6

polyelectrolyte gel thus serves as a common substrate linking bioenergetics (murburn), resting potential (Donnan-Tamagawa) and propagation (the present model): three aspects of a single physical object seen from three disciplinary vantage points.

The principal limitation of the present work is theoretical: the model has not yet been subjected to systematic quantitative fitting against the full HH dataset. Equations (3) – (4) yield numerical predictions for conduction velocity as a function of measurable mechanical parameters (E_{myelin}, r, h), but these predictions have not yet been quantitatively compared with the extensive velocity-diameter data set available for vertebrate nerve fibres. This comparison is a necessary next step.

A second limitation concerns the preparation of the giant squid axon. Because this axon is a fusion of hundreds of smaller axons [5], its hydraulic architecture is unknown. The HH data set, obtained on this preparation, cannot straightforwardly constrain a hydraulic model designed for single-axon geometry. A purpose-designed experimental protocol is required on single myelinated mammalian fibres with intact periaxonal space.

7. Conclusions

The IMH model proposes that the action potential is a coupled ionic-hydraulic phase transition in which mechanical compression triggers K^+ desorption from cytoplasmic gel sites, generating a pressure wave in the periaxonal space. Electrical events are the measurable consequence of this wave, not its cause. The model resolves, without post-hoc adjustment, the 75-year anomaly of Huxley and Stämpfli (1949) [10], accounts for the nearly zero net heat exchange of the action potential [12], and provides a unified physical basis for the universal sigmoidal stimulus-response curve of biological sensors.

Ten falsifiable predictions are presented, each testable with existing or near-existing experimental methods, covering myelin mechanics, mechanoreceptor adaptation, terminal arborisation geometry, motor tremor, conscious perception latency, electrical stimulation, fibre isolation, electromagnetic dipole geometry, axon diameter limits, and velocity-diameter scaling.

The Hodgkin-Huxley model served seven decades with distinction. The IMH model does not request its rejection.

It asks for the experiment.

Author Contributions: Conceptualisation: B.D., H.T., V.M. Theoretical framework and formal analysis: B.D. and V.M. (polyelectrolyte gel foundations), B.D. and H.T. (hydraulic wave mechanics). Writing—original draft: B.D. Writing—review and editing: H.T. and V.M. All authors have read and agreed to the submitted version of the manuscript.

Funding: This research did not receive external funding.

Acknowledgments: The intellectual genealogy of this work begins with SomaSimple, a forum created by the first author where clinicians and researchers daily faced the dissonance between classical electrophysiology and living patients. SomaSimple was the space in which the question was first posed clearly: if the HH model is correct, why does clinical neuroscience fail so consistently to predict the behaviour of the living nervous system? It was on ResearchGate, however, that the exchanges proved most scientifically fertile: Vladimir Matveev deposited his work on Ling's gel theory there, introducing the first author to a framework capable of answering the question SomaSimple had raised. ResearchGate also provided the channel through which the connection with Hirohisa Tamagawa was established and through which sustained exchanges with Ennio Pannese (1928–2025) and Thomas Heimburg enriched the model's anatomical and thermodynamic foundations. The authors thank Ennio Pannese in particular, whose meticulous neurocytological documentation of the axon-Schwann cell couple informed Section 2.4, and who responded to detailed anatomical queries with generosity and precision up to the end of his life.

Preceding Work: This manuscript extends and contextualises an earlier study by the same authors:
Delalande, B.; Tamagawa, H.; Matveev, V. From Nernst to Bernstein and Beyond. *Preprints* **2020**, 2020080529. doi:10.20944/preprints202008.0529.v2

 doi:10.20944/preprints202603.0725.v6

AI Assistance Statement: The authors used large language model (LLM) assistants (Claude, Anthropic) during the preparation of this manuscript for tasks that included literature search, LaTeX editing, and paragraph writing. All scientific content, theoretical claims, and conclusions are the sole responsibility of the authors. The authors have reviewed and verified all AI-assisted content.

Conflicts of Interest: The authors declare no conflicts of interest.

References

1. Nernst, W. Zur Kinetik der in Lösung befindlichen Körper. *Z. Phys. Chem.* **1888**, *2*, 613–637.
2. Bernstein, J. Untersuchungen zur Thermodynamik der bioelektrischen Ströme. *Pflügers Arch.* **1902**, *92*, 521–562.
3. Hodgkin, A.L.; Huxley, A.F. A quantitative description of membrane current and its application to conduction and excitation in nerve. *J. Physiol.* **1952**, *117*, 500–544.
4. Baker, P.F.; Hodgkin, A.L.; Shaw, T.I. Replacement of the axoplasm of giant nerve fibres with artificial solutions. *J. Physiol.* **1962**, *164*, 330–354.
5. Young, J.Z. Structure of nerve fibres and synapses in some invertebrates. *Cold Spring Harb. Symp. Quant. Biol.* **1936**, *4*, 1–6.
6. Ling, G.N. *A Physical Theory of the Living State*; Blaisdell: New York, NY, USA, 1962.
7. Tamagawa, H.; Morita, S. Membrane potential generated by ion adsorption. *Membranes* **2014**, *4*, 257–274.
8. Hofmeister, F. Zur Lehre von der Wirkung der Salze. *Arch. Exp. Pathol. Pharmakol.* **1888**, *24*, 247–260.
9. Heimburg, T.; Jackson, A.D. On soliton propagation in biomembranes and nerves. *Proc. Natl. Acad. Sci. USA* **2005**, *102*, 9790–9795.
10. Huxley, A.F.; Stämpfli, R. Evidence for saltatory conduction in peripheral myelinated nerve fibres. *J. Physiol.* **1949**, *108*, 315–339.
11. Hodgkin, A.L. Evidence for electrical transmission in nerve. Part I. *J. Physiol.* **1937**, *90*, 183–210. doi:10.1113/jphysiol.1937.sp003507.
12. Tasaki, I.; Iwasa, K. Rapid mechanical and thermal changes in the garfish olfactory nerve associated with a propagated impulse. *Biophys. J.* **1982**, *36*, 1–10.
13. Masson, J.-B.; Gallot, G. A model for thermal exchange in axons during action potential propagation. *Eur. Biophys. J.* **2008**, *37*, 1001–1006. doi:10.1007/s00249-008-0329-5.
14. Özbek, S.; Balasubramanian, P.G.; Holstein, T.W. Cnidocyst structure and the biomechanics of discharge. *Toxicon* **2009**, *54*, 1038–1045. doi:10.1016/j.toxicon.2009.03.006.
15. von Uexküll, J. *Umwelt und Innenwelt der Tiere*; Springer: Berlin, Germany, 1909.
16. Pannese, E. *Neurocytology: Fine Structure of Neurons, Nerve Processes and Neuroglial Cells*; Thieme: Stuttgart, Germany, 1994.
17. Damasio, A. *Feeling and Knowing*; Pantheon Books: New York, NY, USA, 2021.
18. Rvachev, M.M. On axoplasmic pressure waves and their possible role in nerve impulse propagation. *Biophys. Rev. Lett.* **2010**, *5*, 73–88. doi:10.1142/S1793048010001147.
19. Barz, H.; Schreiber, A.; Barz, U. Impulses and pressure waves cause excitement and conduction in the nervous system. *Med. Hypotheses* **2013**. PMID: 23953966.
20. Dubey, S.; Bhembre, N.; Bodas, S.; Ghose, A.; Callan-Jones, A.; Pullarkat, P.A. The axonal actin-spectrin lattice acts as a tension buffering shock absorber. *eLife* **2020**, *9*, e51772. doi:10.7554/eLife.51772.
21. Peets, T.; Tamm, K.; Engelbrecht, J. On mathematical modeling of the propagation of a wave ensemble within an individual axon. *Front. Cell. Neurosci.* **2023**, *17*, 1222785. doi:10.3389/fncel.2023.1222785.
22. Carrillo, N. Models of the nerve impulse. In *The Routledge Handbook of Philosophy of Scientific Modeling*; Routledge: London, UK, **2024**; pp. 549–560. doi:10.4324/9781003205647-46
23. Drukarch, B.; Wilhelmus, M.M.M. Thinking about the action potential: the nerve signal as a window to the physical principles guiding neuronal excitability. *Front. Cell. Neurosci.* **2023**, *17*, 1232020. doi:10.3389/fncel.2023.1232020.
24. Delalande, B.; Tamagawa, H.; Matveev, V. Physical inconsistencies in the Hodgkin-Huxley model at the nanoscale. *Preprints* **2026**, 2026030870. doi:10.20944/preprints202603.0870.v1
25. Waxman, S.G.; Bennett, M.V.L. Relative conduction velocities of small myelinated and non-myelinated fibres in the central nervous system. *Nature New Biol.* **1972**, *238*, 217–219.
26. Hursh, J.B. Conduction velocity and diameter of nerve fibers. *Am. J. Physiol.* **1939**, *127*, 131–139.
27. Rushton, W.A.H. A theory of the effects of fibre size in medullated nerve. *J. Physiol.* **1951**, *115*, 101–122.

 doi:10.20944/preprints202603.0725.v6

28. Manoj, K.M.; Jaeken, L. Synthesis of theories on cellular powering, coherence, homeostasis and electromechanics: Murburn concept & evolutionary perspectives. *J. Cell. Physiol.* **2023**, *238*, 931–953. doi:10.1002/jcp.31000.
29. Manoj, K.M.; Tamagawa, H. Critical analysis of explanations for cellular homeostasis and electrophysiology from murburn perspective. *J. Cell. Physiol.* **2021**, *237*, 421–435. doi:10.1002/jcp.30578.
30. Manoj, K.M.; Gideon, D.A.; Bazhin, N.M.; Tamagawa, H.; Nirusimhan, V.; Kavdia, M.; Jaeken, L. Na,K-ATPase: A murzyme facilitating thermodynamic equilibriums at the membrane-interface. *J. Cell. Physiol.* **2023**, *238*, 109–136. doi:10.1002/jcp.30925.
31. Arancibia-Cárcamo, I.L.; Ford, M.C.; Cossell, L.; Ishida, K.; Tohyama, K.; Attwell, D. Node of Ranvier length as a potential regulator of myelinated axon conduction speed. *eLife* **2017**, *6*, e23329. doi:10.7554/eLife.23329.
32. Arancibia-Cárcamo, I.L.; Attwell, D. The node of Ranvier in CNS pathology. *Acta Neuropathol.* **2014**, *128*, 161–175. doi:10.1007/s00401-014-1305-z.
33. Delalande, B.; Tamagawa, H.; Matveev, V. Molecular Foundations of the IMH Model: The V→U Membrane Actuator. *Preprint* **2026**. doi:10.5281/zenodo.19159360
34. Laage, D.; Elsaesser, T.; Hynes, J.T. Water dynamics in the hydration shells of biomolecules. *Chem. Rev.* **2017**, *117*, 10694–10725. doi:10.1021/acs.chemrev.6b00765.
35. Heimburg, T. The mechanical properties of nerves, the size of the action potential, and consequences for the brain. *Chem. Phys. Lipids* **2025**, *267*, 105461. doi:10.1016/j.chemphyslip.2024.105461.
36. Iwasa, K.; Tasaki, I.; Gibbons, R.C. Swelling of nerve fibers associated with action potentials. *Science* **1980**, *210*, 338–339. doi:10.1126/science.7423196.
37. Gonzalez-Perez, A.; Mosgaard, L.D.; Budvytyte, R.; Villagran-Vargas, E.; Jackson, A.D.; Heimburg, T. Solitary electromechanical pulses in lobster neurons. *Biophys. Chem.* **2016**, *216*, 51–59. doi:10.1016/j.bpc.2016.06.005.
38. Ling, T.; Boyle, K.C.; Zuckerman, V.; Flores, T.; Ramakrishnan, C.; Deisseroth, K.; Palanker, D. High-speed interferometric imaging reveals dynamics of neuronal deformation during the action potential. *Proc. Natl. Acad. Sci. USA* **2020**, *117*, 10278–10285. doi:10.1073/pnas.1920039117.
39. Tasaki, I.; Iwasa, K. Shortening of nerve fibers associated with propagated nerve impulses. *Biochem. Biophys. Res. Commun.* **1980**, *94*, 716–720. doi:10.1016/0006-291X(80)91286-3.
40. Tasaki, I.; Byrne, P.M. Tetanic contraction of the crab nerve evoked by repetitive stimulation. *Biochem. Biophys. Res. Commun.* **1982**, *106*, 1435–1440. doi:10.1016/0006-291X(82)91244-7.
41. Heimburg, T. The effect of stretching on nerve excitability. *Hum. Mov. Sci.* **2022**, *86*, 103000. doi:10.1016/j.humov.2022.103000.
42. Tamm, K.; Peets, T.; Engelbrecht, J. On hyperbolicity for nerve pulse propagation in axons. *J. Comput. Neurosci.* **2026**. doi:10.1007/s10827-026-00933-w.
43. Cohen, C.C.H.; Popovic, M.A.; Klooster, J.; Weil, M.-T.; Möbius, W.; Nave, K.-A.; Kole, M.H.P. Saltatory conduction along myelinated axons involves a periaxonal nanocircuit. *Cell* **2020**, *180*, 311–322. doi:10.1016/j.cell.2019.11.039.
44. Beaudoin, C.A.; Salvage, S.C.; Hamaia, S.W.; Lei, M.; Huang, C.L.-H.; Jackson, A.P. Structural electrobiology: architecture of the bioelectric code. *Open Biol.* **2025**, *15*, 240379. doi:10.1098/rsob.240379.
45. Aggarwal, S.; Snaidero, N.; Pähler, G.; Frey, S.; Sánchez, P.; Zweckstetter, M.; Janshoff, A.; Schneider, A.; Weil, M.-T.; Schaap, I.A.T.; Görlich, D.; Simons, M. Myelin membrane assembly is driven by a phase transition of myelin basic proteins into a cohesive protein meshwork. *PLoS Biol.* **2013**, *11*, e1001577. doi:10.1371/journal.pbio.1001577.
46. Zuchero, J.B.; Fu, M.-M.; Sloan, S.A.; Ibrahim, A.; Olson, A.; Zaremba, A.; Dugas, J.C.; Wienbar, S.; Caprariello, A.V.; Kantor, C.; Leonoudakis, D.; Lariosa-Willingham, K.; Kronenberg, G.; Gertz, K.; Soderling, S.H.; Miller, R.H.; Barres, B.A. CNS myelin wrapping is driven by actin disassembly. *Dev. Cell* **2015**, *34*, 152–167. doi:10.1016/j.devcel.2015.06.011.
47. Nawaz, S.; Sánchez, P.; Schmitt, S.; Snaidero, N.; Mitkovski, M.; Velte, C.; Brückner, B.R.; Alexopoulos, I.; Czopka, T.; Jung, S.Y.; Rhee, J.S.; Janshoff, A.; Witke, W.; Schaap, I.A.T.; Lyons, D.A.; Simons, M. Actin filament turnover drives leading edge growth during myelin sheath formation in the central nervous system. *Dev. Cell* **2015**, *34*, 139–151. doi:10.1016/j.devcel.2015.06.004.
48. Snaidero, N.; Möbius, W.; Czopka, T.; Hekking, L.H.P.; Mathisen, C.; Verkleij, D.; Goebbels, S.; Edgar, J.; Merkler, D.; Lyons, D.A.; Nave, K.-A.; Simons, M. Myelin membrane wrapping of CNS axons by PI(3,4,5)P_3-dependent polarized growth at the inner tongue. *Cell* **2014**, *156*, 277–290. doi:10.1016/j.cell.2013.11.044.

 doi:10.20944/preprints202603.0725.v6

49. Velumian, A.A.; Samoilova, M.; Fehlings, M.G. Visualization of cytoplasmic diffusion within living myelin sheaths of CNS white matter axons using microinjection of the fluorescent dye Lucifer Yellow. *Neuroimage* **2011**, *56*, 27–34. doi:10.1016/j.neuroimage.2010.11.022.
50. Frey, S.; Richter, R.P.; Görlich, D. FG-rich repeats of nuclear pore proteins form a three-dimensional meshwork with hydrogel-like properties. *Science* **2006**, *314*, 815–817. doi:10.1126/science.1132516.
51. Matsumoto, G.; Ichikawa, M.; Tasaki, A.; Murofushi, H.; Sakai, H. Axonal microtubules necessary for generation of sodium current in squid giant axons. I. Pharmacological study on sodium current and restoration of sodium current by microtubule proteins and 260K protein. *J. Membr. Biol.* **1984**, *77*, 77–91. doi:10.1007/BF01872758.
52. Matsumoto, G.; Ichikawa, M.; Tasaki, A. Axonal microtubules necessary for generation of sodium current in squid giant axons. II. Effect of colchicine upon asymmetrical displacement current. *J. Membr. Biol.* **1984**, *77*, 93–99. doi:10.1007/BF01872759.
53. Terakawa, S. Potential-dependent variations of the intracellular pressure in the intracellularly perfused squid giant axon. *J. Physiol.* **1985**, *369*, 229–248. doi:10.1113/jphysiol.1985.sp015898.
54. Chuang, Y.-C.; Alcantara, A.; Fabris, G.; Abderezaei, J.; Lu, T.-A.; Melendez-Vasquez, C.V.; Kurt, M. Myelination dictates axonal viscoelasticity. *Eur. J. Neurosci.* **2023**, *57*, 1225–1240. doi:10.1111/ejn.15954.
55. Rosso, G.; Liashkovich, I.; Gess, B.; Young, P.; Kun, A.; Shahin, V. Unravelling crucial biomechanical resilience of myelinated peripheral nerve fibres provided by the Schwann cell basal lamina and PMP22. *Sci. Rep.* **2014**, *4*, 7286. doi:10.1038/srep07286.
56. Urbanski, M.M.; Brendel, M.B.; Melendez-Vasquez, C.V. Acute and chronic demyelinated CNS lesions exhibit opposite elastic properties. *Sci. Rep.* **2019**, *9*, 999. doi:10.1038/s41598-018-37745-7.